JOURNAL OF COMPUTATIONAL PHYSICS 50, 360–408 (1983)

Three-Dimensional Computer Modeling of Electromagnetic Fields: A Global Lookback Lattice Truncation Scheme*

RICHARD W. ZIOLKOWSKI, NIEL K. MADSEN, AND ROBERT C. CARPENTER

Lawrence Livermore National Laboratory, University of California, Livermore, California 94550

Received March 25, 1982; revised November 2, 1982

A new lattice truncation scheme for the finite difference time domain approach to the solution of Maxwell's equations has been developed. The problem space is truncated near the sources and the field components on its boundary are generated from those field values known at retarded times on an interior surface one cell from it with an integral representation of the electromagnetic field. The numerical implementation of this global lookback scheme is discussed. Examples which have been used to determine its characteristics and its validity are given.

1. INTRODUCTION

An approach to the modeling of time dependent elctromagnetic problems which may involve nonlinear, anisotropic, and inhomogeneous media effects is a self-consistent finite difference time domain (FD-TD) solution of Maxwell's equations. The FD-TD approach is attractive because it exchanges the complexity of those problems for labor by a computer. Various FD-TD techniques and successes have been documented [1–13].

Approximate solution of Maxwell's curl equations in Cartesian geometry is accomplished with the FD-TD approach by discretizing the problem space whose coordinates are (x, y, z) into a finite difference lattice composed of rectangular cells with dimensions $(\Delta x, \Delta y, \Delta z)$ and by discretizing time into invervals of length Δt. A space-time point on the lattice is defined to be (x_i, y_j, z_k, t_n); hence, it can be labeled simply by its indices (i, j, k, n). The components of the electric and magnetic field vectors are positioned about a cell of the lattice as shown in Fig. 1. The finite difference approximations of those equations are given in Fig. 2. The electric and magnetic fields are evaluated at alternate half-time steps. This permits integration of the FD-TD equations forward in time in the usual "leapfrog" fashion as illustrated in Fig. 3. Furthermore, centered difference expressions can be used for both the space and time

* This work was supported under the auspices of the U.S. Department of Energy by the Lawrence Livermore National Laboratory under Contract W-7405-ENG-48.

0021-9991/83 $3.00

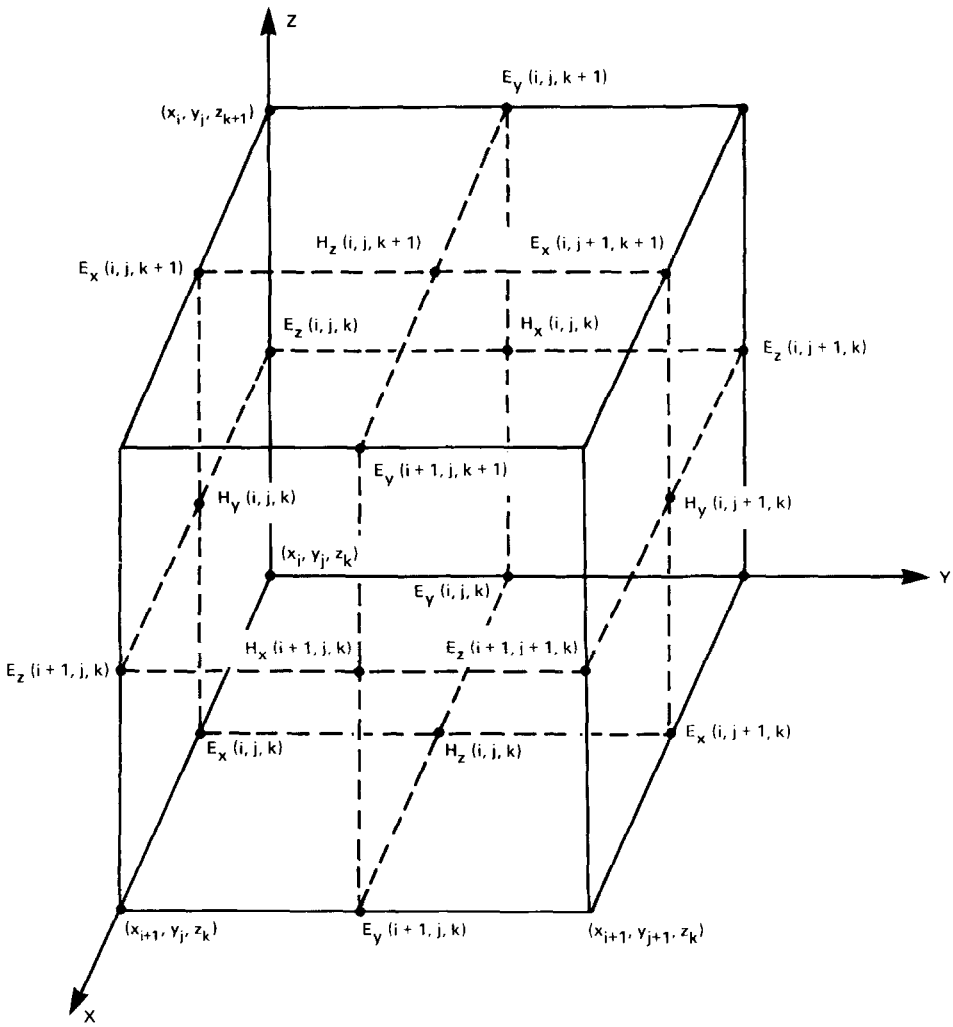

FIG. 1. Positions of the field components about a unit cell of the finite difference lattice.

derivatives to achieve second-order accuracy in the space and time increments without requiring simultaneous equations to compute the fields at the latest time step.

The (explicit) finite difference method has several practical difficulties. To ensure accuracy of the computed spatial derivatives, the cell size must be sufficiently small compared to a wavelength. However, to guarantee the stability of the time-stepping algorithm, the Courant stability condition must be satisfied: The lattice spacings $\Delta x, \Delta y$, and Δz must be chosen so that $(R/\Delta t) \geqslant v$, where the distance parameter $R = (\Delta x^{-2} + \Delta y^{-2} - \Delta z^{-2})^{-1/2}$; i.e., the velocity of numerical signals in the lattice must not be less than the velocity of light in the medium being modeled. Thus,

because of computer time and expense limitations, there is a limit to the number of time steps, hence, fine details (maximum resolution = one cell) one can model in a problem. Subsequently, numerical dispersion occurs because signals whose wavelengths are smaller than a unit cell size are not propagated in the lattice (high-frequency trapping). Furthermore, because of computer storage limitations, the lattice must be truncated to a finite size. However, the field components at the lattice truncation planes cannot be determined directly from the differenced curl equations. They must be computed using an auxiliary truncation condition.

Proper truncation of the lattice requires that any outward-travelling waves disappear at the lattice boundary without significant reflection during the repeated time stepping of the algorithm. Improper truncation would cause errors for all time steps after the spurious numerical reflections return to the vicinity of the observation point. This is illustrated in Fig. 4. Since Maxwell's equations are hyperbolic, causal information is propagated from a point in a forward light cone. A signal from P reaches the improperly truncated lattice boundary S at $t = \tau_1$; its reflected signal reaches P at $t = \tau_2$. For closed region problems where the boundary is a perfectly conducting metal, the truncation conditions are straightforward: the tangential electric and normal magnetic fields at the conducting surfaces are zero. For open region problems existing codes treat the truncation only approximately. The standard approximate truncation or boundary schemes include [3–17]:

Maxwell's Equations

$$\mu\partial_t H_x + \sigma^* H_x = -(\partial_y E_z - \partial_z E_y) - K_x, \qquad \mu\partial_t H_y + \sigma^* H_y = -(\partial_z E_x - \partial_x E_z) - K_y,$$
$$\mu\partial_t H_z + \sigma^* H_z = -(\partial_x E_y - \partial_y E_x) - K_z,$$
$$\varepsilon\partial_t E_x + \sigma E_x = (\partial_y H_z - \partial_z H_y) - J_x, \qquad \varepsilon\partial_t E_y + \sigma E_y = (\partial_z H_x - \partial_x H_z) - J_y$$
$$\varepsilon\partial_t E_z + \sigma E_z = (\partial_x H_y - \partial_y H_x) - J_z$$

Field Component Locations (lattice size $= N_x \Delta x \times N_y \Delta y \times N_z \Delta z$)

$$H_x^n(i,j,k) = H_x(x_i, y_{j+1/2}, z_{k+1/2}, n\,\Delta t)$$
$$i = 1,\ldots,N_x + 1, \quad j = 1,\ldots,N_y, \quad k = 1,\ldots,N_z;$$
$$H_y^n(i,j,k) = H_x(x_{i+1/2}, y_j, z_{k+1/2}, n\,\Delta t)$$
$$i = 1,\ldots,N_x, \quad j = 1,\ldots,N_y + 1, \quad k = 1,\ldots,N_z;$$
$$H_z^n(i,j,k) = H_z(x_{i+1/2}, y_{j+1/2}, z_k, n\,\Delta t)$$
$$i = 1,\ldots,N_x, \quad j = 1,\ldots,N_y, \quad k = 1,\ldots,N_z + 1;$$
$$E_x^n(i,j,k) = E_x(x_{i+1/2}, y_j, z_k, (n+1/2)\,\Delta t)$$
$$i = 1,\ldots,N_x, \quad j = 1,\ldots,N_y + 1, \quad k = 1,\ldots,N_z + 1;$$
$$E_y^n(i,j,k) = E_y(x_i, y_{j+1/2}, z_k, (n+1/2)\,\Delta t)$$
$$i = 1,\ldots,N_x + 1, \quad j = 1,\ldots,N_y, \quad k = 1,\ldots,N_z + 1;$$
$$E_z^n(i,j,k) = E_z(x_i, y_j, z_{k+1/2}, (n+1/2)\,\Delta t)$$
$$i = 1,\ldots,N_x + 1, \quad j = 1,\ldots,N_y + 1, \quad k = 1,\ldots,N_z.$$

FIG. 2. Three-dimensional FD-TD equations in rectangular coordinates.

Finite Difference Equations (nonuniform grid allowed)

$$H_x^n(i,j,k) = \alpha_m H_x^{n-1}(i,j,k) - \beta_m K_x^{n-1} - \beta_m \left\{ \frac{E_z^{n-1}(i,j+1,k) - E_z^{n-1}(i,j,k)}{y_{j+1} - y_j} \right\} + \beta_m \left\{ \frac{E_y^{n-1}(i,j,k+1) - E_y^{n-1}(i,j,k)}{z_{k+1} - z_k} \right\},$$

$$H_y^n(i,j,k) = \alpha_m H_y^{n-1}(i,j,k) - \beta_m K_y^{n-1} - \beta_m \left\{ \frac{E_x^{n-1}(i,j,k+1) - E_x^{n-1}(i,j,k)}{z_{k+1} - z_k} \right\} + \beta_m \left\{ \frac{E_z^{n-1}(i+1,j,k) - E_z^{n-1}(i,j,k)}{x_{i+1} - x_i} \right\},$$

$$H_z^n(i,j,k) = \alpha_m H_z^{n-1}(i,j,k) - \beta_m K_z^{n-1} - \beta_m \left\{ \frac{E_y^{n-1}(i+1,j,k) - E_y^{n-1}(i,j,k)}{x_{i+1} - x_i} \right\} + \beta_m \left\{ \frac{E_x^{n-1}(i,j+1,k) - E_x^{n-1}(i,j,k)}{y_{j+1} - y_j} \right\},$$

$$E_x^n(i,j,k) = \alpha_e E_x^{n-1}(i,j,k) - \beta_e J_x^{n-1} + \beta_e \left\{ \frac{H_z^{n-1}(i,j,k) - H_z^{n-1}(i,j-1,k)}{y_{j+1/2} - y_{j-1/2}} \right\} - \beta_e \left\{ \frac{H_y^{n-1}(i,j,k) - H_y^{n-1}(i,j,k-1)}{z_{k+1/2} - z_{k-1/2}} \right\},$$

$$E_y^n(i,j,k) = \alpha_e E_y^{n-1}(i,j,k) - \beta_e J_y^{n-1} + \beta_e \left\{ \frac{H_x^{n-1}(i,j,k) - H_x^{n-1}(i,j,k-1)}{z_{k+1/2} - z_{k-1/2}} \right\} - \beta_e \left\{ \frac{H_z^{n-1}(i,j,k) - H_z^{n-1}(i-1,j,k)}{x_{i+1/2} - x_{i-1/2}} \right\},$$

$$E_z^n(i,j,k) = \alpha_e E_z^{n-1}(i,j,k) - \beta_e J_z^{n-1} + \beta_e \left\{ \frac{H_y^{n-1}(i,j,k) - H_y^{n-1}(i-1,j,k)}{x_{i+1/2} - x_{i-1/2}} \right\} - \beta_e \left\{ \frac{H_x^{n-1}(i,j,k) - H_x^{n-1}(i,j-1,k)}{y_{j+1/2} - y_{j-1/2}} \right\},$$

where

$$\alpha_m = \left(\frac{\mu}{\Delta t} - \frac{\sigma^*}{2}\right) \Big/ \left(\frac{\mu}{\Delta t} + \frac{\sigma^*}{2}\right), \qquad \beta_m = \left(\frac{\mu}{\Delta t} + \frac{\sigma^*}{2}\right)^{-1}$$

and $(K_x^{n-1}, K_y^{n-1}, K_z^{n-1})$ are all evaluated at the desired H-component locations, and where

$$\alpha_e = \left(\frac{\varepsilon}{\Delta t} - \frac{\sigma}{2}\right) \Big/ \left(\frac{\varepsilon}{\Delta t} + \frac{\sigma}{2}\right), \qquad \beta_e = \left(\frac{\varepsilon}{\Delta t} + \frac{\sigma}{2}\right)^{-1}$$

and $(J_x^{n-1}, J_y^{n-1}, J_z^{n-1})$ are all evaluated at the desired E-component locations. In free-space

$$\bar{J} = \bar{K} = 0, \qquad \sigma = \sigma^* = 0,$$

$$\alpha_e = \alpha_m = 1, \qquad \beta_e = \frac{\Delta t}{\varepsilon_0}, \qquad \beta_m = \frac{\Delta t}{\mu_0}.$$

FIG. 2—*Continued.*

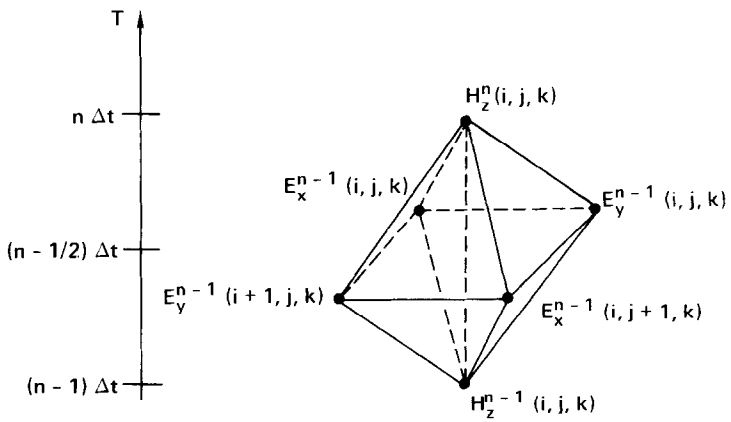

$$H_z^n(i, j, k) = H_z^{n-1}(i, j, k) - \frac{\Delta t}{\mu_0}\left\{\frac{E_y^{n-1}(i + 1, j, k) - E_y^{n-1}(i, j, k)}{x_{i+1} - x_i}\right\} + \frac{\Delta t}{\mu_0}\left\{\frac{E_x^{n-1}(i, j + 1, k) - E_x^{n-1}(i, j, k)}{y_{j+1} - y_j}\right\}$$

FIG. 3. "Leapfrog FD-TD representation" of the free-space Maxwell curl equation $-\mu_0 \partial_t H_z = \partial_x E_y - \partial_y E_x$.

(1) Large simulation volume. The problem space is made large enough to generate solutions within a required time window before reflections from the inadequately treated boundaries arrive at the observation point.

(2) Absorptive boundaries. An isotropic, lossy medium is introduced in the region exterior to the lattice boundary to aid in reducing the effective reflection coefficient of the lattice truncation planes. An anisotropic electric loss σ_{ext} and an anisotropic magnetic loss σ_{ext}^* are commonly specified there; they appear only in the curl equations

$$\text{curl } \bar{H} = \sigma_{ext}\bar{E} + \varepsilon_0 \partial \bar{E}/\partial t, \qquad \text{curl } \bar{E} = -\sigma_{ext}^* \bar{H} - \mu_0 \partial \bar{H}/\partial t,$$

where ε_0 and μ_0 are, respectively, the free-space permittivity and permeability. The wave is reduced in amplitude upon reaching the lattice truncations and is progressively damped as its remnants reverberate between the lattice planes. Since the effective steady-state wave impedance of this medium is

$$Z = [(i\omega\mu_0 - \sigma_{ext}^*)/(i\omega\varepsilon_0 - \sigma_{ext})]^{1/2},$$

selecting $\sigma_{ext}^* = \mu_0 \sigma_{ext}/\varepsilon_0$ reduces it to the free-space impedance $Z_0 = (\mu_0/\varepsilon_0)^{1/2}$.

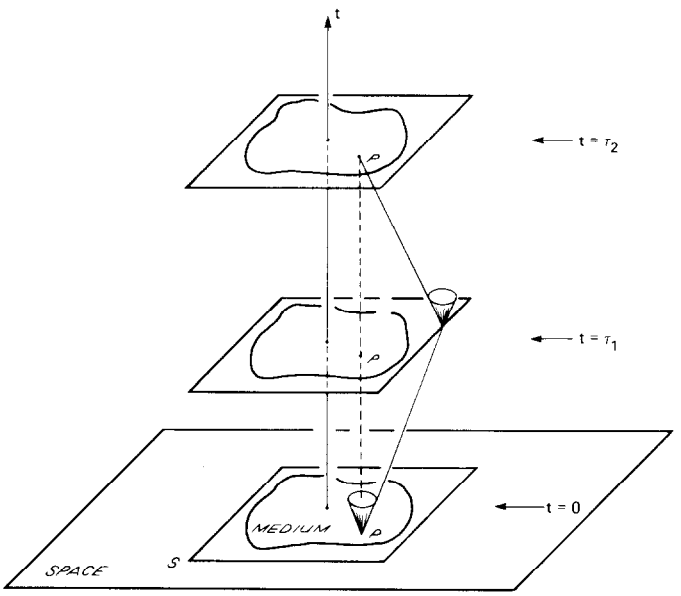

FIG. 4. Truncation boundary reflections.

(3) Field matching techniques. The boundary field values are extrapolated from cells adjacent to the boundary with approximate formulas. Lookback and impedance outer boundary schemes are commonly employed. The former is usually based on a far-field approximation; i.e., far from any sources the fields look like spherical waves

$$\bar{H} = f(t - r/c)(\hat{h}/r), \qquad \bar{E} = Z_0 f(t - r/c)(\hat{e}/r),$$

where the unit vectors $\hat{e} = \hat{h} \times \hat{r}$ and $\hat{r} = \bar{r}/r$, $\bar{r}$ being the position vector of the observation point. This scheme is also known as the "radiating boundary condition." It is a lookback scheme because the retarded time values of the fields at interior points must be used. The impedance scheme assumes simply that $\bar{E} = Z_0(\bar{H} \times \bar{r})$ on the outer boundary; i.e., that the field locally looks like an outward traveling plane wave. Other matching schemes such as averaging over field values at neighboring lattice points have also been utilized. In addition, several local, higher order approximate schemes have been developed [17–20].

The approximations these standard schemes incorporate create certain inherent deficiencies. The large simulation volume scheme has excessively large storage requirements to achieve late observation times. Reflections, although significantly reduced in magnitude with the absorptive boundary scheme, are still present in the FD-TD lattice. The radiating boundary scheme necessitates the mating of a spherical wave representation to the Cartesian lattice. It requires a large simulation volume to be rigorous because the electromagnetic field is approximated accurately by a

spherical wave only very far from its source. Because locally only a minute portion of a general wave front resembles a plane wave, the impedance boundary scheme is valid only in a very fine lattice. The latter (because of the Courant stability condition) requires an excessively large number of computational time cycles to achieve late observation times.

To overcome many of these imperfections, a new accurate treatment of the lattice truncation conditions for three-dimensional open region problems has been developed. This scheme is based upon the numerical implementation of a discrete form of an exact global lookback representation of the electromagnetic field. The mathematical formulation of this global lookback scheme and its numerical implementation will be discussed, respectively, in Sections 2 and 3. The examples used to validate the resultant algorithm will be examined in Section 4. A summary of the results and suggestions for future investigations are given in Section 5.

2. Exact Global Lookback Representation

Consider the representation of an electromagnetic field in terms of its values on a closed surface [21]. The physical problem space is divided into two separate volumes U and V as shown in Fig. 5. The closed surface S is the boundary of those regions; its normal $\bar{n}$ points into V. The interior region U encompasses all of the sources and medium inhomogeneities, nonlinearities, and anisotropies. The observation point $\bar{r}$ lies in the free-space exterior region V. The point $\bar{s}$ lies on S. Assuming that the fields satisfy the Sommerfeld radiation condition and for the moment that electric and magnetic currents $(\bar{J}, \bar{K})$ and charge densities (ρ_e, ρ_m) are located in V, the electric field at $\bar{r}$ at time t is given by the expression [21]

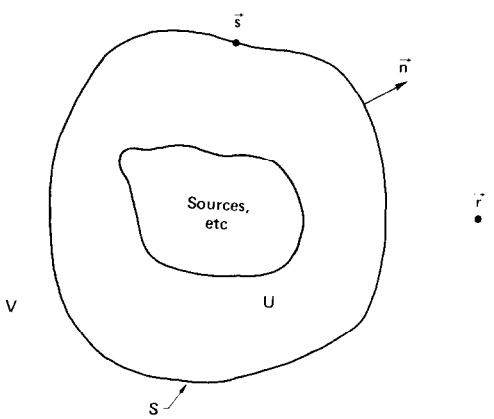

FIG. 5. Geometry of the exact global lookback representation of the field.

$$\bar{E}(\bar{r},t)=\int_V dV\,\theta(t_R)\left\{\frac{[\rho_e]\,\hat{R}}{4\pi\varepsilon R^2}+\frac{[\partial_t\rho_e]\,\hat{R}}{4\pi\varepsilon Rc}-\frac{\mu[\partial_t\bar{J}]}{4\pi R}\right\}$$
$$+\int_V dV\,\theta(t_R)\frac{\hat{R}}{4\pi R}\times\left\{\frac{[\bar{K}]}{R}+\frac{[\partial_t\bar{K}]}{c}\right\}$$
$$-\int_S dS\,\theta(t_R)\left\{\frac{\bar{n}}{4\pi R}\times[\partial_t\mu\bar{H}]-\frac{[\bar{n}\times\bar{E}]\times\hat{R}}{4\pi R^2}-\frac{[\bar{n}\times\partial_t\bar{E}]\times\hat{R}}{4\pi Rc}\right.$$
$$\left.-\frac{[\bar{n}\cdot\bar{E}]\,\hat{R}}{4\pi R^2}-\frac{[\bar{n}\cdot\partial_t\bar{E}]\,\hat{R}}{4\pi Rc}\right\},\tag{2.1}$$

where $\partial_t\equiv\partial/\partial t$ and the step function

$$\begin{aligned}\theta(x)&=1, \quad \text{if} \quad x>0,\\ &=0, \quad \text{if} \quad x<0,\end{aligned}\tag{2.2}$$

and where

$$R=|\bar{r}-\bar{s}|,\tag{2.3}$$
$$\hat{R}=(\bar{r}-\bar{s})/R,\tag{2.4}$$
$$\tau=R/c,\tag{2.5}$$
$$t_R=t-\tau,\tag{2.6}$$
$$[f]=f(\bar{s},t_R).\tag{2.7}$$

The volume integral terms represent the contributions to the field from the source distributions within V. The surface integral represents the contributions to the field of the sources not in V. The magnetic field representation is obtained by duality

$$\bar{E}\to\bar{H}\to-\bar{E}, \qquad \bar{J}\to\bar{K}\to-\bar{J},$$
$$\rho_e\to\rho_m\to-\rho_e, \qquad \varepsilon\to\mu\to\varepsilon.$$

Since V is considered to be free space, the source terms are identically zero and the field expressions reduce to

$$\bar{E}(\bar{r},t)=\int_S dS\,\frac{\theta(t_R)}{4\pi}\left\{(\bar{n}\times[\bar{E}+\tau\partial_t\bar{E}])\times\frac{\hat{R}}{R^2}\right.$$
$$\left.+(\bar{n}\cdot[\bar{E}+\tau\partial_t\bar{E}])\frac{\hat{R}}{R^2}-\frac{\bar{n}\times[\partial_t\mu_0\bar{H}])}{R}\right\},\tag{2.8}$$

$$\bar{H}(\bar{r},t)=\int_S dS\,\frac{\theta(t_R)}{4\pi}\left\{(\bar{n}\times[\bar{H}+\tau\partial_t\bar{H}])\times\frac{\hat{R}}{R^2}\right.$$
$$\left.+(\bar{n}\cdot[\bar{H}+\tau\partial_t\bar{H}])\frac{\hat{R}}{R^2}+\frac{\bar{n}\times[\partial_t\varepsilon_0\bar{E}]}{R}\right\}.\tag{2.8′}$$

Note that those source terms would be needed if a field/particle problem were considered that allowed particles in V.

A particular component of the fields (2.8) and (2.8′) is obtained by considering their projections onto the desired direction. Let $\bar{p}$ represent the unit vector along that direction at the observation point. The desired expressions are $\bar{p} \cdot \bar{E}(\bar{r}, t)$ and $\bar{p} \cdot \bar{H}(\bar{r}, t)$. With several vector identity manipulations they can be represented as

$$\bar{p} \cdot \bar{E}(\bar{r}, t) = \int_S dS \frac{\theta(t_R)}{4\pi} \bar{n} \cdot \left\{ (\bar{p} \cdot [\bar{E} + \tau \partial_t \bar{E}]) \frac{\hat{R}}{R^2} + (\bar{p} \times [\bar{E} + \tau \partial_t \bar{E}]) \times \frac{\hat{R}}{R^2} + \frac{\bar{p} \times [\partial_t \mu_0 \bar{H}]}{R} \right\}, \tag{2.9}$$

$$\bar{p} \cdot \bar{H}(\bar{r}, t) = \int_S dS \frac{\theta(t_R)}{4\pi} \bar{n} \cdot \left\{ (\bar{p} \cdot [\bar{H} + \tau \partial_t \bar{H}]) \frac{\hat{R}}{R^2} + (\bar{p} \times [\bar{H} + \tau \partial_t \bar{H}]) \times \frac{\hat{R}}{R^2} - \frac{\bar{p} \times [\partial_t \varepsilon_0 \bar{E}]}{R} \right\}. \tag{2.9′}$$

The explicit components corresponding to Eqs. (2.9) and (2.9′) are given in Appendix A.

Equations (2.9) and (2.9′) have the following symmetry properties: Let $\bar{p}_i$ $(i = 1, 2, 3)$ represent, respectively, the unit vectors $\hat{x}$, $\hat{y}$, and $\hat{z}$. Thus, the term $\bar{p}_i \cdot \bar{E} = E_i$ is the ith component of the electric field. With more vector manipulations Eq. (2.9) can then be rewritten as

$$E_i(\bar{r}, t) = \sum_{j=1}^{3} \{\hat{A}_i^j(\bar{r}, \bar{s}; t) E_j(\bar{s}, t_R) + \mu_0 \hat{B}_i^j(\bar{r}, \bar{s}; t) H_j(\bar{s}, t_R)\}, \tag{2.10}$$

where the operators

$$\hat{\sigma}_i^j(\bar{r}, \bar{s}; t) = \int_S dS \frac{\theta(t - \tau)}{4\pi} \frac{(\bar{n} \cdot \hat{R})}{R^2} (\bar{p}_i \cdot \bar{p}_j)\{\mathrm{ID} + \tau \partial_t\}, \tag{2.11}$$

$$\hat{\alpha}_i^j(\bar{r}, \bar{s}; t) = \int_S dS \frac{\theta(t - \tau)}{4\pi} \left\{ \frac{(\hat{R} \times \bar{n})}{R^2} \cdot (\bar{p}_i \times \bar{p}_j) \right\} \{\mathrm{ID} + \tau \partial_t\} \tag{2.12}$$

(ID is the identity operator) are such that

$$\hat{A}_i^j = \hat{\sigma}_i^j + \hat{\alpha}_i^j \tag{2.13}$$

and the operator

$$\hat{B}_i^j(\bar{r}, \bar{s}; t) = \int_S dS \frac{\theta(t - \tau)}{4\pi} \left\{ \frac{\bar{n}}{R} \cdot (\bar{p}_i \times \bar{p}_j) \right\} \{\partial_t\}. \tag{2.14}$$

Clearly, the operator $\hat{\sigma}_i^j$ is symmetric $(\hat{\sigma}_i^j = \hat{\sigma}_j^i)$ and diagonal $(\bar{p}_i \cdot \bar{p}_j = \delta_{ij}$, Kronecker's delta). On the other hand, the operators $\hat{\alpha}_i^j$ and $\hat{B}_i^j$ are antisymmetric

(e.g., $\hat{\alpha}_i^j = -\hat{\alpha}_j^i$). The same symmetry relations pertain to the analogous version of Eq. (2.9′),

$$H_i(\bar{r}, t) = \sum_{j=1}^{3} \{\hat{A}_i^j(\bar{r}, \bar{s}; t) * H_j(\bar{s}, t_R) - \varepsilon_0 \hat{B}_i^j(\bar{r}, \bar{s}; t) * E_j(\bar{s}, t_R)\}. \tag{2.15}$$

Notice that expressions (2.9) and (2.9′) constitute an exact global lookback representation of the electromagnetic field resulting from sources enclosed by S. They are lookback expressions because the field values at any point $\bar{r}$ in V are calculated from field values on S at retarded times. Furthermore, they exhibit a global dependence; a field component at $\bar{r}$ is calculated from field values at every point on S. The FD-TD lattice truncation scheme to be described in Section 3 is formulated with discrete versions of these exact global lookback expressions.

3. Numerical Implementation

An FD-TD lattice truncation scheme that is based upon the exact global lookback expressions has been constructed with an approach analogous to the successful technique formulated by McDonald and Wexler [22] for elliptic problems. As shown in Fig. 6, a boundary surface S (a rectangular cylinder for the Cartesian lattice) is specified that closely surrounds the region of interest. The electric or magnetic field values on the outer boundary surface Σ which is located in free-space one cell away from S, are respectively calculated with discretized versions of Eq. (2.9) and (2.9′). Thus, the field values on Σ are determined from the field values on S at retarded times. Since the field values on Σ are supplied external to the FD-TD solution

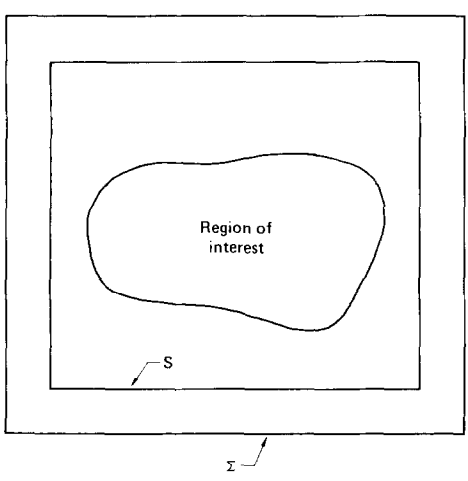

FIG. 6. Exact global lookback scheme configuration.

process, they effectively truncate the FD-TD lattice. The particular choice of which field components should be specified on Σ depends on the representation of the sources within S. As will be discussed in Section 4, it was found numerically that electric (magnetic) dipole sources can be properly represented in the FD-TD lattice by specifying magnetic (electric) field values on a small surface within S surrounding the dipole location and that the lattice is properly truncated by specifying the same field components on Σ.

Note that because it incorporates Eqs. (2.9) and (2.9′), this lattice truncation technique is a global lookback scheme. The global lookback scheme is particularly appealing because it eliminates the need for a large simulation volume. The surface S can be placed in close proximity to the region of interest, the surface Σ being separated from it by one cell. Furthermore, unlike most standard schemes, it is based upon an exact representation of the field, not an approximate one.

The calculational flow of the FD-TD process is analogous to the one employed in Holland's THREDE code [3]. Major modifications of that code were made to accommodate the global lookback scheme. Although only a uniform lattice was actually considered in the validation problems, the implementation of that scheme included the nonuniform lattice capability of the original THREDE code.

To compute any of the desired field values (E_x, E_y, E_z) or (H_x, H_y, H_z) at their appropriate locations on Σ (for example, the values of E_x and E_y on the faces of Σ, where $z = \text{constant}$), a complete surface integral over the surface S of the inner concentric rectangular cylinder must be performed. Both of the integrals (2.9) and (2.9′) consist of six distinct integrals, one over each of the six faces of S. Each of those faces is already decomposed into rectangular patches or zones by the FD-TD lattice. Thus, those integrals are calculated in a local manner zone by zone, and the results are summed to generate the entire surface integral.

Both of the surface integrals (2.9) and (2.9′) required all six field component values $(E_x, E_y, E_z; H_x, H_y, H_z)$ on S at times from the current time value t backwards in time to the maximum retarded time value

$$t_{R\max} = t - (R_{\max})/c, \tag{3.1}$$

where if the outer surface Σ has the dimensions $(N_x \Delta x, N_y \Delta y, N_z \Delta z)$ measured from the origin (x_1, y_1, z_1),

$$R_{\max} = [(x_{N_x} - x_2)^2 + (y_{N_y} - y_2)^2 + (z_{N_z} - z_2)^2]^{1/2} \tag{3.2}$$

the length of the diagonal from a corner of S to an opposite corner of Σ. All of these field values are computed and stored at all of the points on the inner surface S where the zone lines intersect. To obtain the field values at a zone-line intersection, the usual field values which exist at the centers of the zone edges and faces are averaged according to the following scheme: Referring to Fig. 7a, if the field values are known at the mid-edge points (b and d) and the distances between the zone line points (a, c)

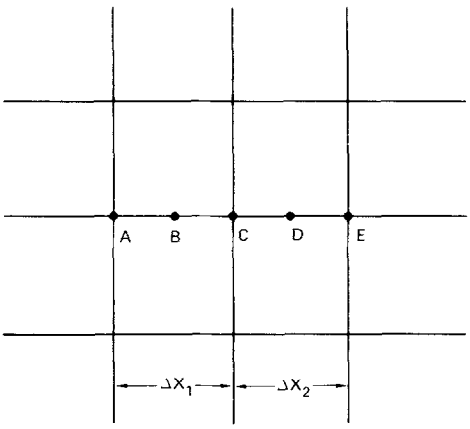

FIG. 7a. Two-term field component averaging.

and (c, e) are, respectively, Δx_1 and Δx_2, the desired field values at the point $c, f(c)$, is computed from the field values $f(b)$ and $f(d)$ as

$$f(c) = \frac{f(b) \cdot \Delta x_2 + f(d) \cdot \Delta x_1}{\Delta x_2 + \Delta x_1}. \tag{3.3}$$

Similarly, referring to Fig. 7b, if the field values are known at the zone center points 1, 2, 3, and 4 and the distances between the zone-line intersection points (a, b), (b, e), (b, c), and (c, d) are, respectively, Δy_1, Δy_2, Δx_1, and Δx_2, the desired field value at c is taken to be

$$f(c) = \frac{g(1, 3) \cdot \Delta x_2 + g(2, 4) \cdot \Delta x_1}{\Delta x_1 + \Delta x_2}, \tag{3.4}$$

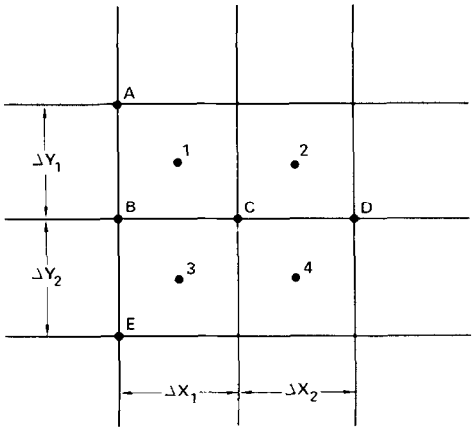

FIG. 7b. Four-term field component averaging.

where

$$g(1,3)=\frac{f(1)\cdot\Delta y_2+f(3)\cdot\Delta y_1}{\Delta y_1+\Delta y_2} \tag{3.5a}$$

and

$$g(2,4)=\frac{f(2)\cdot\Delta y_2+f(4)\cdot\Delta y_1}{\Delta y_1+\Delta y_2} \tag{3.5b}$$

The required time derivatives of the field components are generated by accessing the two back-stored values of the field which bracket the retarded time of interest and then numerically differentiating (dividing the two values by Δt). To avoid ambiguity, if a time derivative value at one of the past lattice time points is needed, the convention of using the slope to the left of the desired time point was adopted.

The surface integral over a zone face is calculated by evaluating the integrand at each of the four corners of the zone face. Next, an approximating bilinear function is fit using the four integrand corner values and the zone integral is then easily calculated. Each corner point will have its own field values, R, t_R, etc., hence, its own contribution to the zone integral. Note that many quantities computed for one zone can be saved and utilized for adjacent zones. For example, consider a zone Γ on a face $z=$ constant whose corners are $1=(x_i, y_j)$, $2=(x_{i+1}, y_j)$, $3=(x_i, y_{j+1})$, and $4=(x_{i+1}, y_{j+1})$. The bilinear function

$$I(x,y)=a_0+a_1x+a_2y+a_3xy \tag{3.6}$$

is fit to the corresponding four values of the integrand: I_1, I_2, I_3, and I_4; i.e.,

$$a_0=I_1, \qquad a_1=\frac{I_2-I_1}{\Delta x_i}, \qquad a_2=\frac{I_3-I_1}{\Delta y_j}, \qquad a_4=\frac{I_1-I_2-I_3+I_4}{\Delta x_i\,\Delta y_j}. \tag{3.7}$$

The integral of $I(x,y)$ over that zone is simply

$$\iint_\Gamma I(x,y)\,dx\,dy=(I_1+I_2+I_3+I_4)\frac{\Delta x_i\,\Delta y_j}{4}. \tag{3.8}$$

The desired, total integral over S follows readily.

All of the numerical computations were performed on a Cray-1 computer. The global lookback code, which was only partially optimized, backstored to $t_{R\max}$ every field value. The Cray-1 provided ample memory space to accommodate all of those backstored field values in a problem of modest size. No attempt was made to track the variation between points on Σ of the maximum time backstorage required by the corresponding field value calculations. Furthermore, the global lookback code was not extensively vectorized. The sum over the surface S was performed for each field value at a point on Σ rather than computing all of the values simultaneously (in parallel), hence, summing only once. Other considerations such as incorporating the

symmetry properties given in Section 2 or employing a more general interpolation scheme (the general discretized form of the exact global lookback field representation is given in Appendix B) also were not attempted. Consequently, the code was rather expensive to run. Because our intent was only to verify the validity of the global lookback scheme, a comparison of its cost with any of the standard approximate truncation schemes was not made.

4. Validation

To validate the global lookback algorithm, a three-dimensional problem was sought which had an exact analytical solution. It was felt that it would be inadequate to characterize the behavior of the global lookback scheme with the usual procedure which would compare its results with those obtained with a large simulation volume. The latter is limited by its clear time (the time at which reflections from the outer boundary reach the observation point) and only produces an approximate solution. It was decided that a time-varying electric or magnetic dipole would be a suitable test case.

An electric dipole oriented along the z axis is assumed to be located at the center of the finite difference lattice. Its dipole moment is taken to be

$$\bar{p}(\bar{r}, t) = f(t)\, \delta(\bar{r})\, \hat{z}.$$

The resultant fields are

$$\bar{E}(\bar{r}, t) = \frac{\{3(\hat{r} \cdot \hat{z})\, \hat{r} - \hat{z}\}}{4\pi\varepsilon_0 r^3} [f + \tau \partial_t f] + \frac{\{\hat{r} \times (\hat{r} \times \hat{z})\}}{4\pi\varepsilon_0 c^2 r} [\partial_t^2 f], \tag{4.1}$$

$$\bar{H}(\bar{r}, t) = -\frac{(\hat{r} \times \hat{z})}{4\pi r^2} [\partial_t f + \tau \partial_t^2 f], \tag{4.2}$$

where $c\tau = |\bar{r}| = r$ and $[f] = f(t - \tau)$. Their components are given explicitly in Appendix C.

The first specific problem treated was a smooth turn-on of the field. Since the fields depend at most on the second derivatives of f, this effect is achieved with a function that is zero for $t < 0$, nonzero for $t > 0$, and at least C^2 at $t = 0$. We chose

$$\begin{aligned} f(t) &= 0, & t &< 0, \\ &= 1 - \exp(-\alpha t^3/3), & t &\geqslant 0, \end{aligned} \tag{4.3}$$

where the rise time of the pulse is governed by the real constant α. In all of the examples considered a fast rise time was desired and $\alpha = 2.0 \times 10^{23}$ sec^{-3}. The dipole was located at the center of $9 \times 9 \times 9$ lattice whose cells have the dimensions $\Delta x = \Delta y = \Delta z = 0.5$ m. The time step was set equal to the Courant limit. The electric dipole was represented in the FD-TD lattice by specifying the exact magnetic field

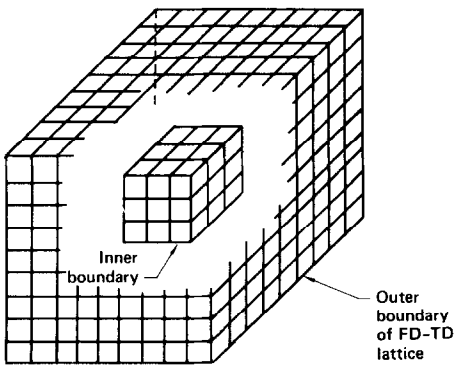

FIG. 8a. Configuration of the dipole field problems.

values (4.2) on the surface of a $3 \times 3 \times 3$ cube centered around its location. This configuration is depicted in Figs. 8a and b. Figure 8b indicates the relative location of the inner boundary, the integration surface S and the outer boundary Σ. Note that this specification is dual to the one employed in scattering problems where the tangential components of the scattered electric field on a perfectly conducting surface are set equal to the negative of the incident electric field. This specification also effectively isolates the field components in the interior of the inner cube; hence, they are set equal to zero. The magnetic fields were calculated at the outer boundary of the lattice with the global lookback scheme (2.9′). Note from Eqs. (4.1) and (4.2) that the magnetic fields are expected to reduce to zero when $f(t)$ reaches its constant value 1 and that the electric fields reach a constant, large nonzero value. Typical results for an "interior" point in the region between the inner and outer boundary away from any of the many symmetry planes and for a point on the outer boundary, as indicated in Fig. 8b, are given, respectively, in Figs. 9 and 10. In particular, the

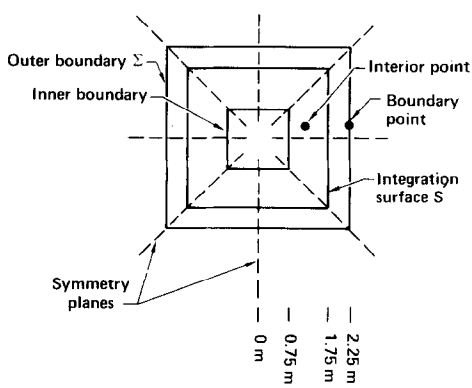

FIG. 8b. Cross-sectional view of the configuration of a dipole field problem.

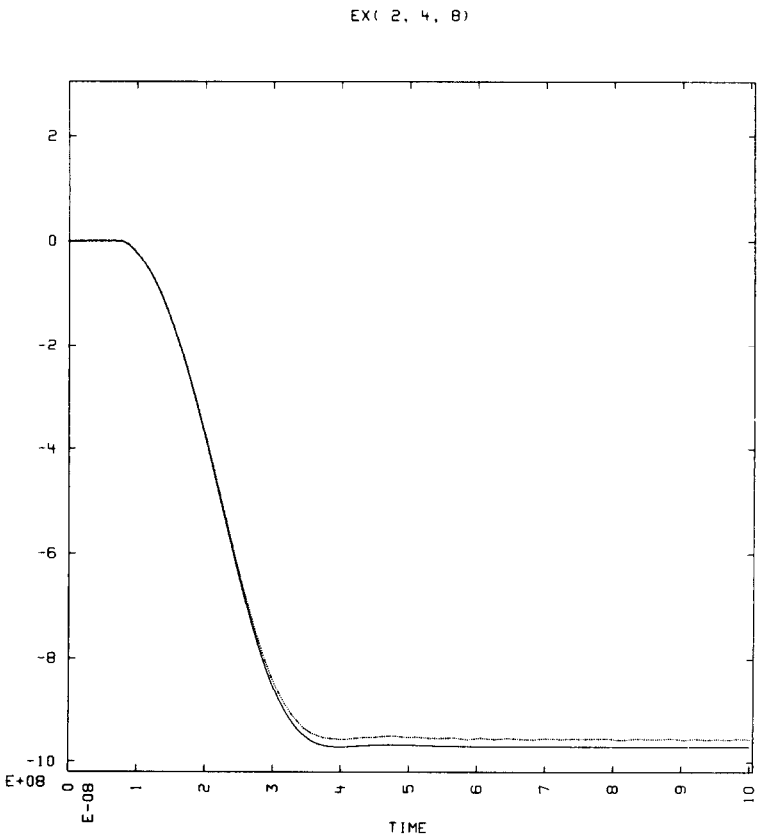

FIG. 9a. Comparison of the exact E_x values (—) with those calculated with the global lookback scheme (···) at an interior point for a turned-on electric dipole.

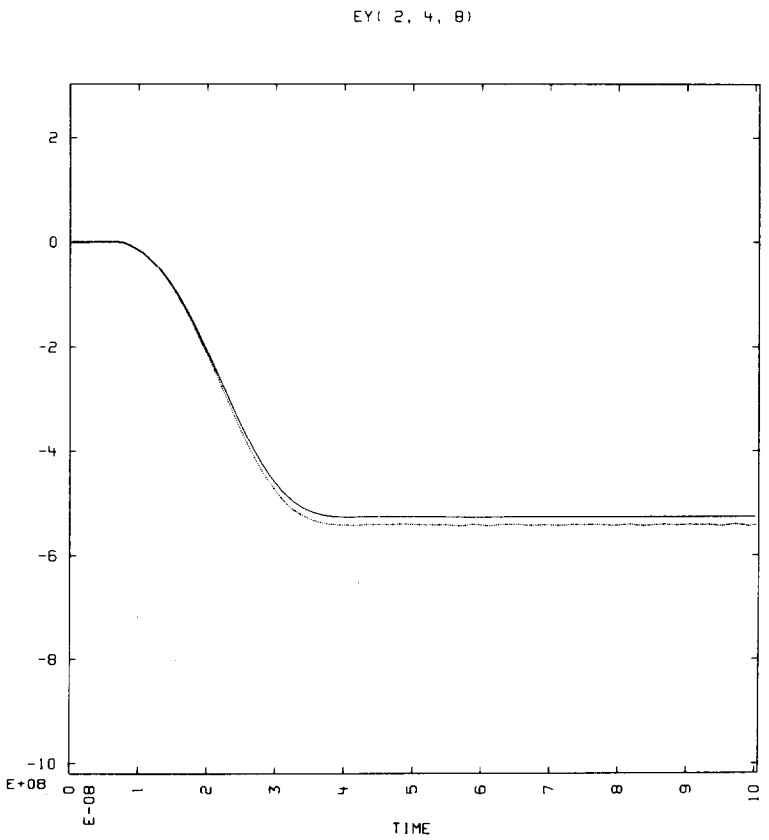

FIG. 9b. Comparison of the exact E_y values (—) with those calculated with the global lookback scheme (···) at an interior point for a turned-on electric dipole.

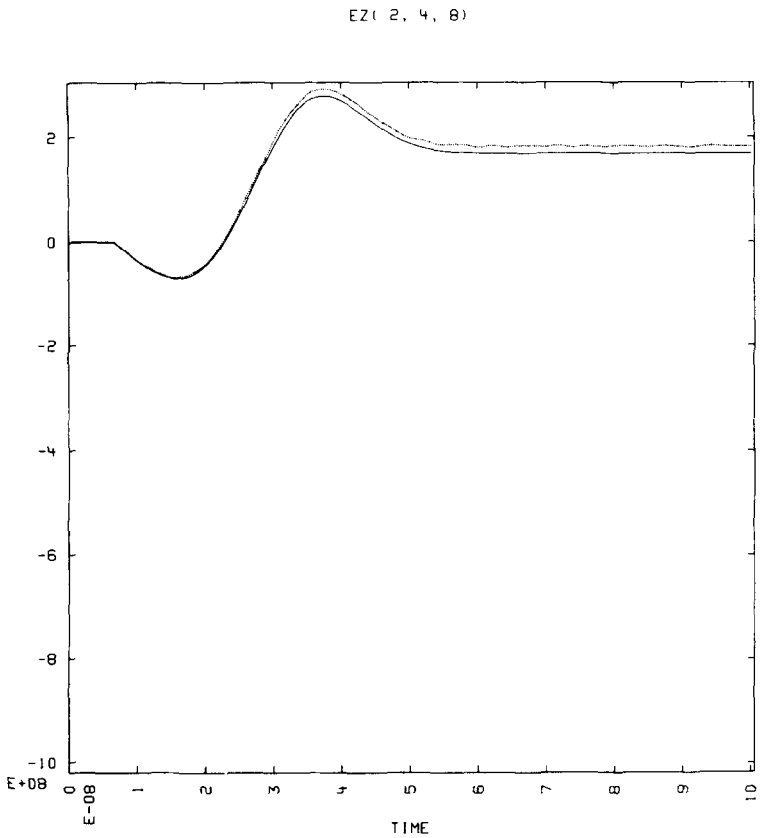

FIG. 9c. Comparison of the exact E_z values (—) with those calculated with the global lookback scheme (···) at an interior point for a turned-on electric dipole.

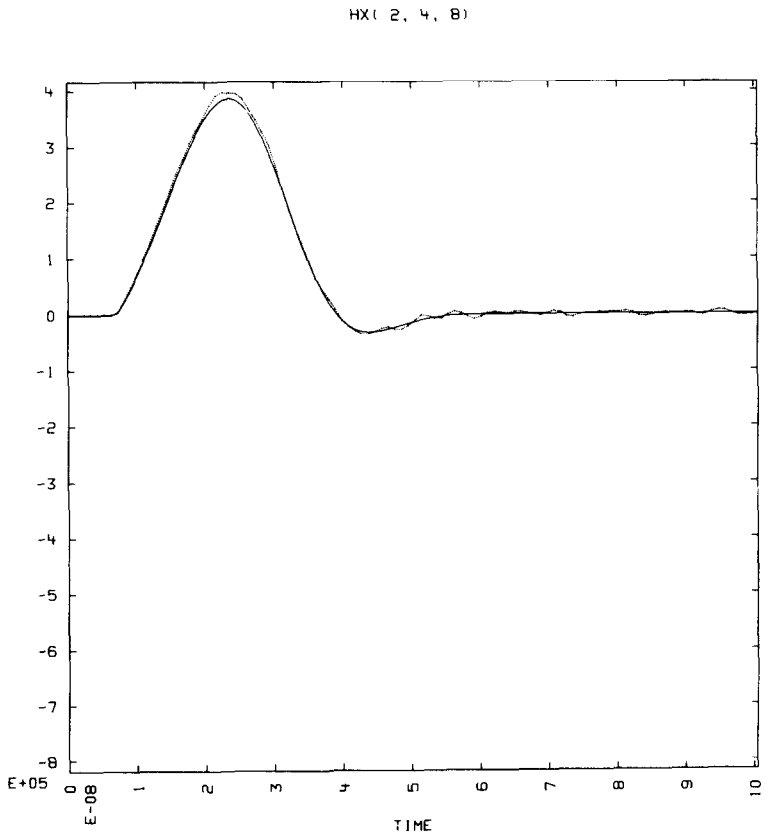

FIG. 9d. Comparison of the exact H_x values (—) with those calculated with the global lookback scheme (···) at an interior point for a turned-on electric dipole.

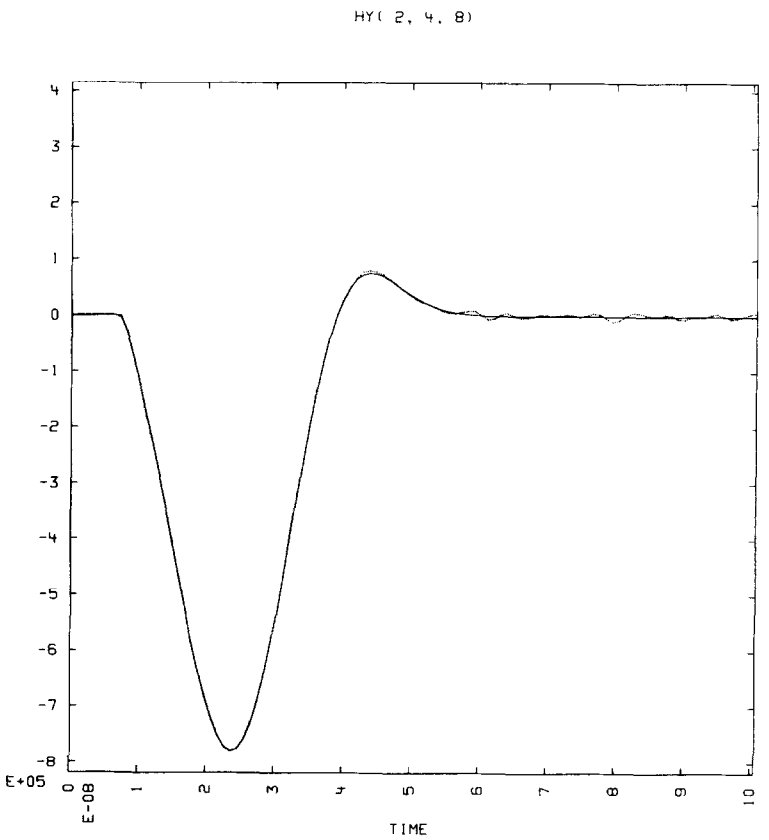

FIG. 9e. Comparison of the exact H_y values (—) with those calculated with the global lookback scheme (···) at an interior point for a turned-on electric dipole.

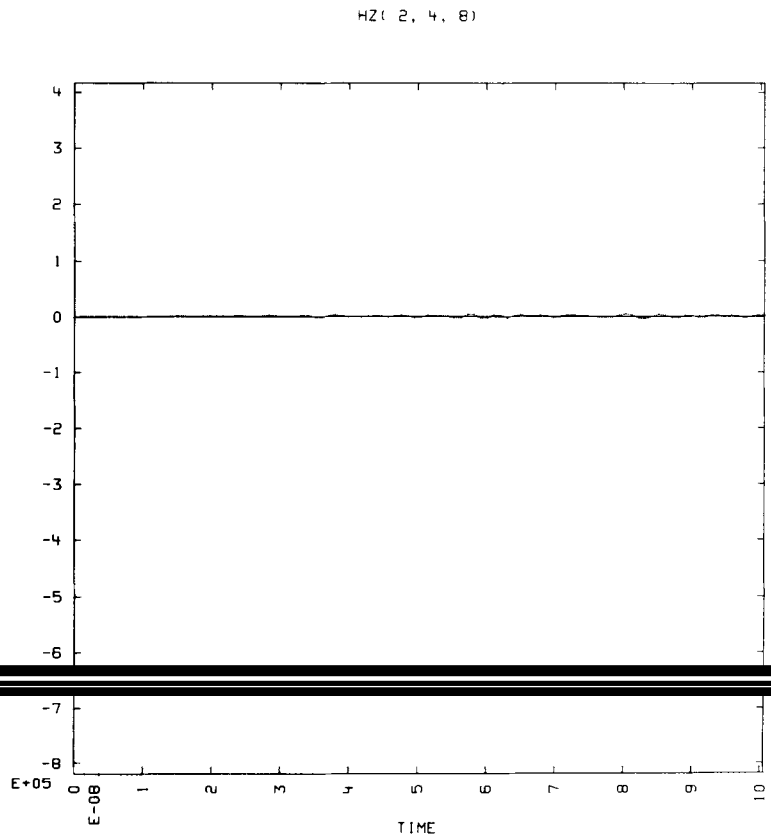

FIG. 9f. Comparison of the exact H_z values (---) with those calculated with the global lookback scheme (···) at an interior point for a turned-on electric dipole.

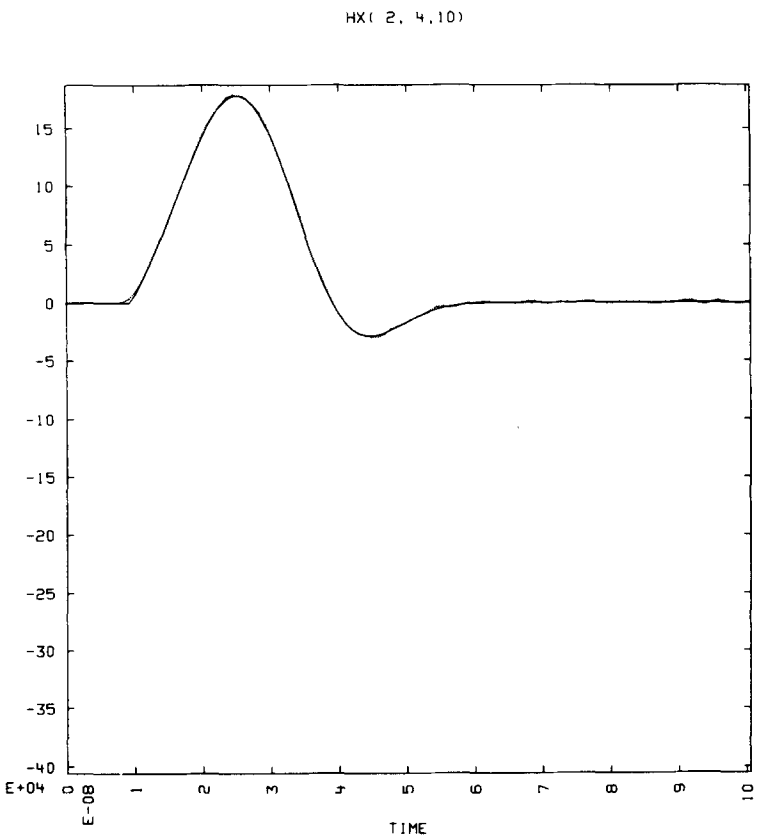

FIG. 10a. Comparison of the exact H_x values (—) with those calculated with the global lookback scheme (···) at a boundary point for a turned-on electric dipole.

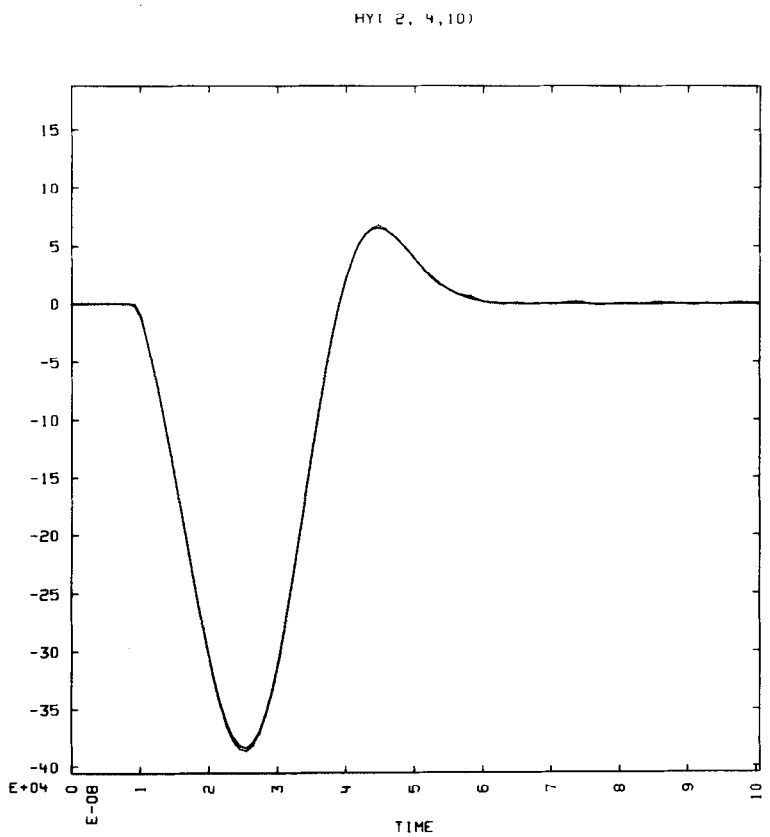

FIG. 10b. Comparison of the exact H_y values (—) with those calculated with the global lookback scheme (···) at a boundary point for a turned-on electric dipole.

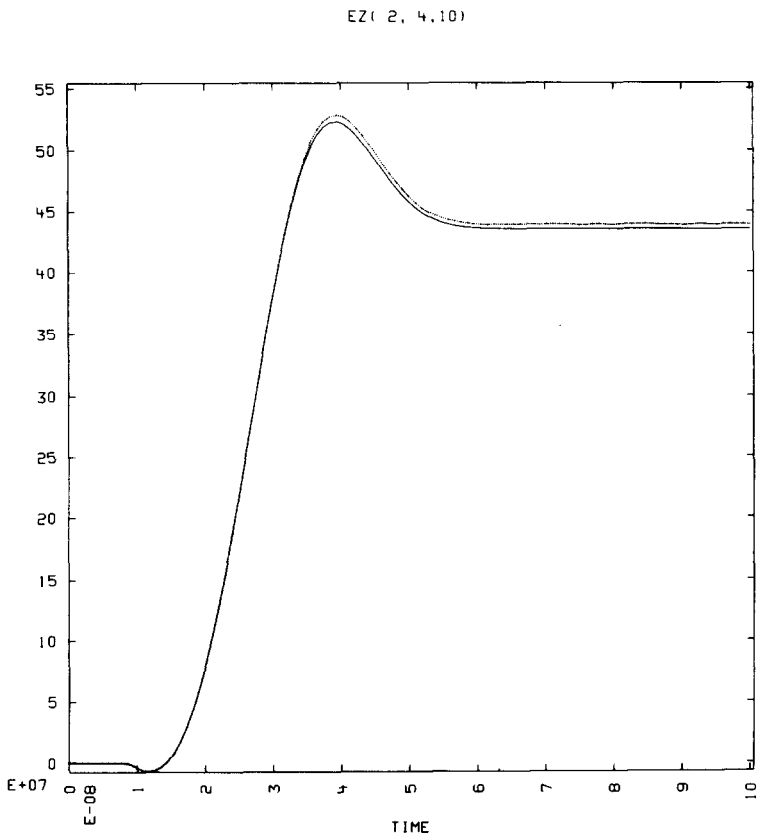

FIG. 10c. Comparison of the exact E_z values (—) with those calculated with the global lookback scheme (···) at a boundary point for a turned-on electric dipole.

boundary point was located on the face of Σ, where $z = +2.25$m. Thus, only the H_x and H_y components were calculated there with the global lookback scheme. The E_z values folow from those components with the FD-TD process. The other components (E_x, E_y, H_z) exist at points outside of Σ and are not computed. The values calculated with the global lookback code are represented by $(\cdots)$, the exact values by (—). The clear time for this problem is at most 10 ns. As shown, excellent agreement is achieved out to 100 ns. Figures 11 and 12 show the fields at the points used in, respectively, Figs. 9 and 10 as computed with the original THREDE code in a $29 \times 29 \times 29$ lattice truncated with null tangential electric field components on its outer boundary surface. Clear time in that case is about 45 ns. The reflections from the outer boundary (which clearly degrade the signal) are apparent.

The second problem studied was one involving a driving function that turned on and off. The response is a pulse that travels through the FD-TD lattice. The particular forcing function was $f(t) = g(\beta t)$, where $\beta = 2.0 \times 10^7$ sec^{-1}, and where

$$\begin{aligned} g(x) &= 0, && x < 0, \quad x > 1, \\ &= 32x^3 - 48x^4, && 0 \leqslant x \leqslant 1/2, \\ &= 32(1-x)^3 - 48(1-x)^4, && 1/2 \leqslant x \leqslant 1. \end{aligned} \tag{4.4}$$

The results at the same point locations as in the first case are given in Figs. 13 and 14. Because of the coarse gridding used, discontinuities seem to appear in the exact fields where the on-to-off transition in $f(t)$ occurs (at $t = 25$ ns). Nonetheless, the global lookback code results approximate the exact solutions extremely well. The oscillations at late times represent high-frequency noise and are also a consequence of the coarse gridding. (Note that lattice resonance oscillations in a lattice with cells of length 0.5 m occur at 300 MHz and with a period of 3.33 ns. The late-time oscillations in the figures coincide with these values.)

Analogous results were obtained for the dual problem: a magnetic dipole with electric field values set on the inner and outer boundaries.

It was discovered unexpectedly that a linear growth appears in certain field components when the specification of the field values on the boundary surfaces is not consistent with the chart shown in Fig. 15. Consider, for instance, the electric dipole problem. If the (exact) electric field values were set on the inner boundary and the magnetic field values were calculated on the outer boundary with the global lookback scheme, the magnetic field components exhibited the linear growth. Furthermore, the effect was more apparent near the inner boundary. Analogous but less severe behavior was also noticed when the electric dipole was represented by magnetic field values on the inner boundary and the lattice was truncated with global lookback electric field values. In this case the effect was more noticeable for points near the outer boundary. Numerical experiments with the global lookback code and with the original THREDE code indicated that this anomalous behaviour was due strictly to truncation errors and not to any code instability. The differences at neighboring lattice points on the inner and/or outer boundary surfaces of the specified electric

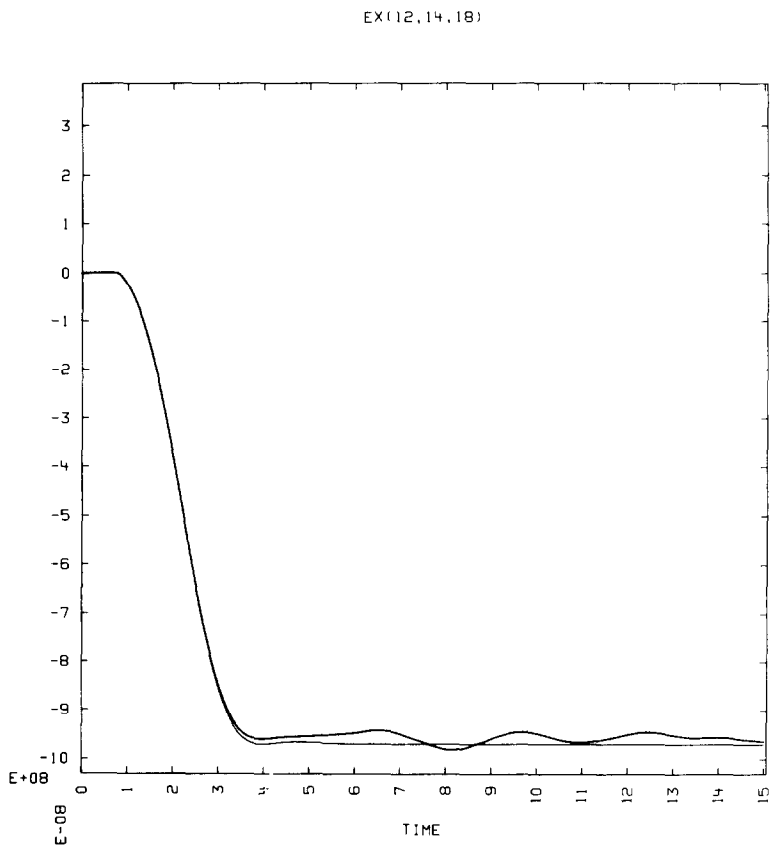

FIG. 11a. Comparison of the exact E_x values (—) with those calculated with a $29 \times 29 \times 29$ lattice and $E_{tan} = 0$ outer boundary condition version of the THREDE code (···) at a point interior to Σ for a turned-on electric dipole.

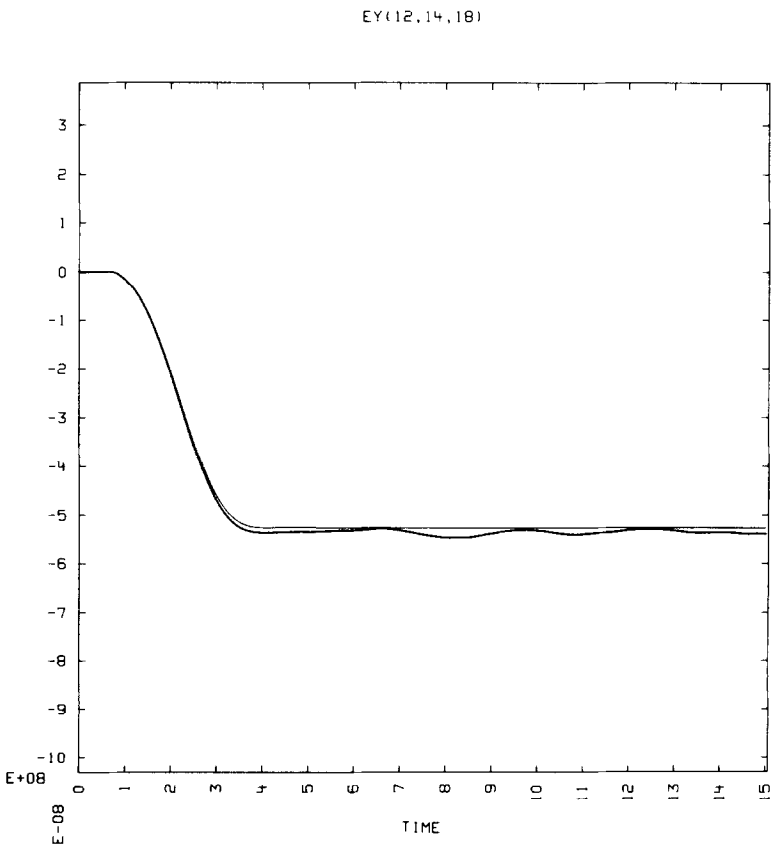

FIG. 11b. Comparison of the exact E_y values (—) with those calculated with a $29 \times 29 \times 29$ lattice and $E_{\tan} = 0$ outer boundary condition version of the THREDE code (···) at a point interior to Σ for a turned-on electric dipole.

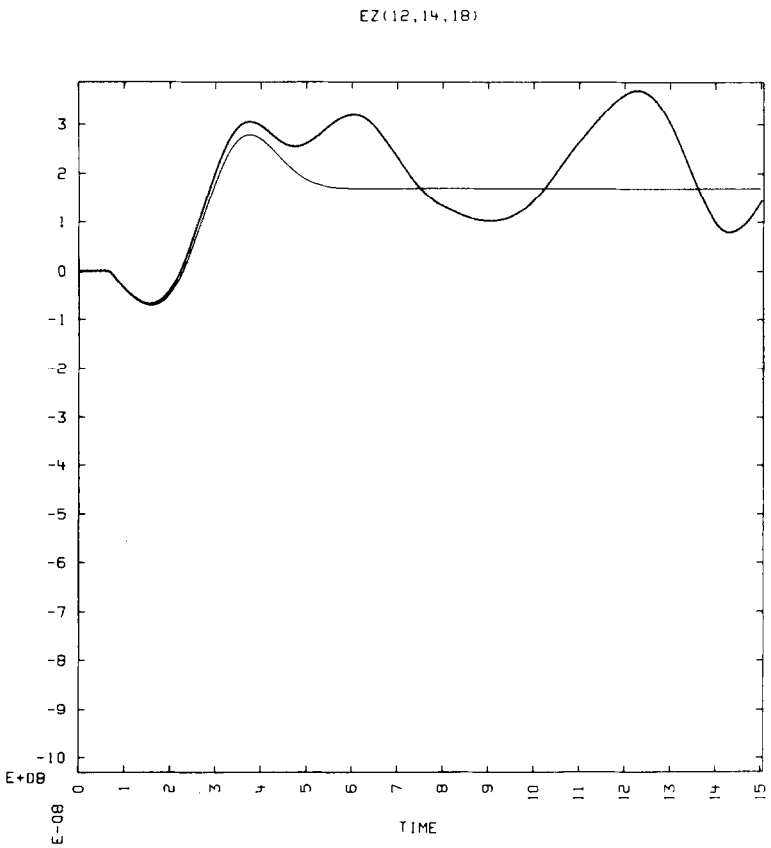

FIG. 11c. Comparison of the exact E_z values (—) with those calculated with a $29 \times 29 \times 29$ lattice and $E_{tan} = 0$ outer boundary condition version of the THREDE code (···) at a point interior to Σ for a turned-on electric dipole.

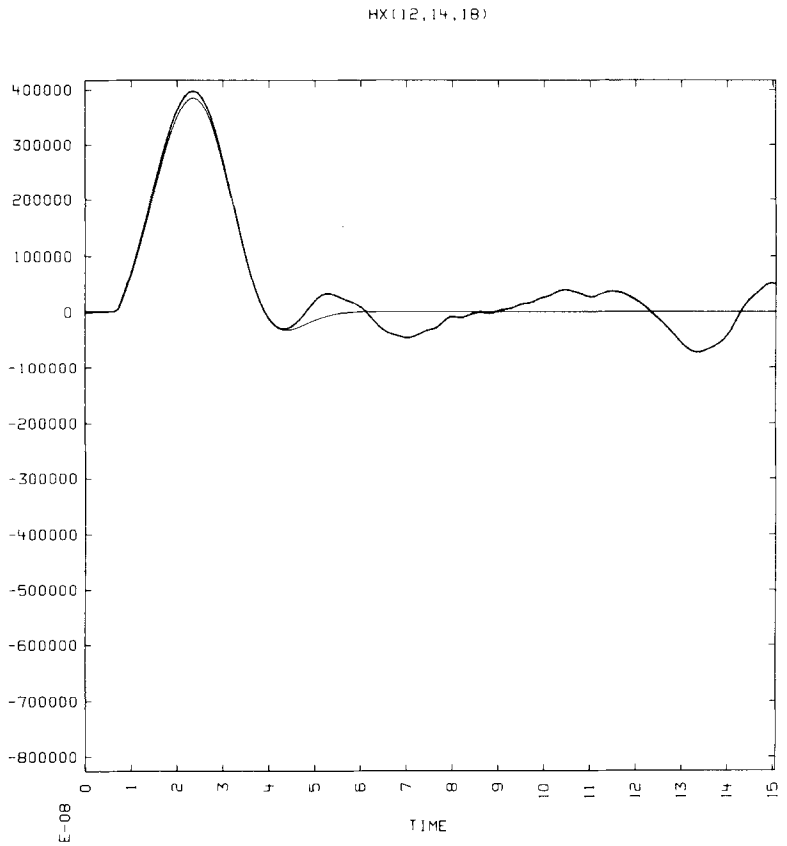

FIG. 11d. Comparison of the exact H_x values (—) with those calculated with a $29 \times 29 \times 29$ lattice and $E_{\tan} = 0$ outer boundary condition version of the THREDE code (···) at a point interior to Σ for a turned-on electric dipole.

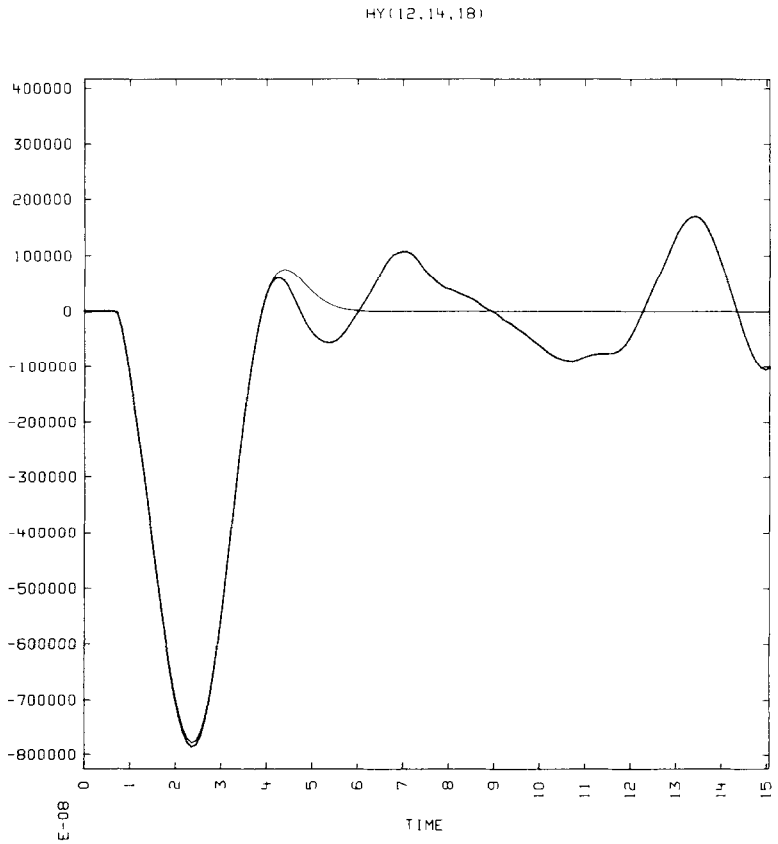

FIG. 11e. Comparison of the exact H_y values (—) with those calculated with a $29 \times 29 \times 29$ lattice and $E_{tan} = 0$ outer boundary condition version of the THREDE code (···) at a point interior to Σ for a turned-on electric dipole.

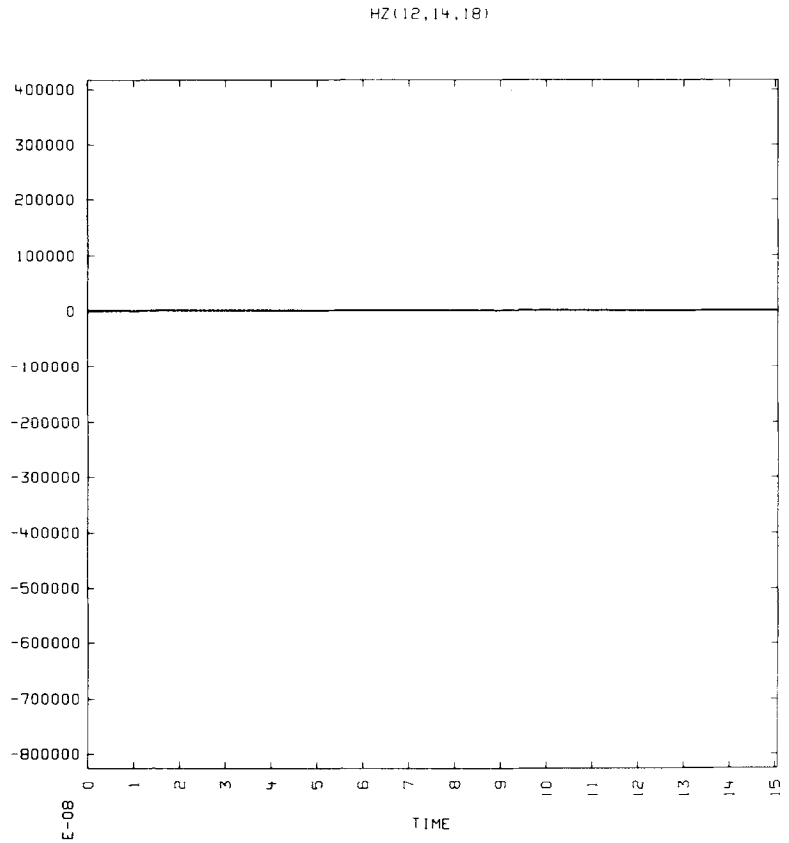

FIG. 11f. Comparison of the exact H_z values (—) with those calculated with a $29 \times 29 \times 29$ lattice and $E_{tan} = 0$ outer boundary condition version of the THREDE code (···) at a point interior to Σ for a turned-on electric dipole.

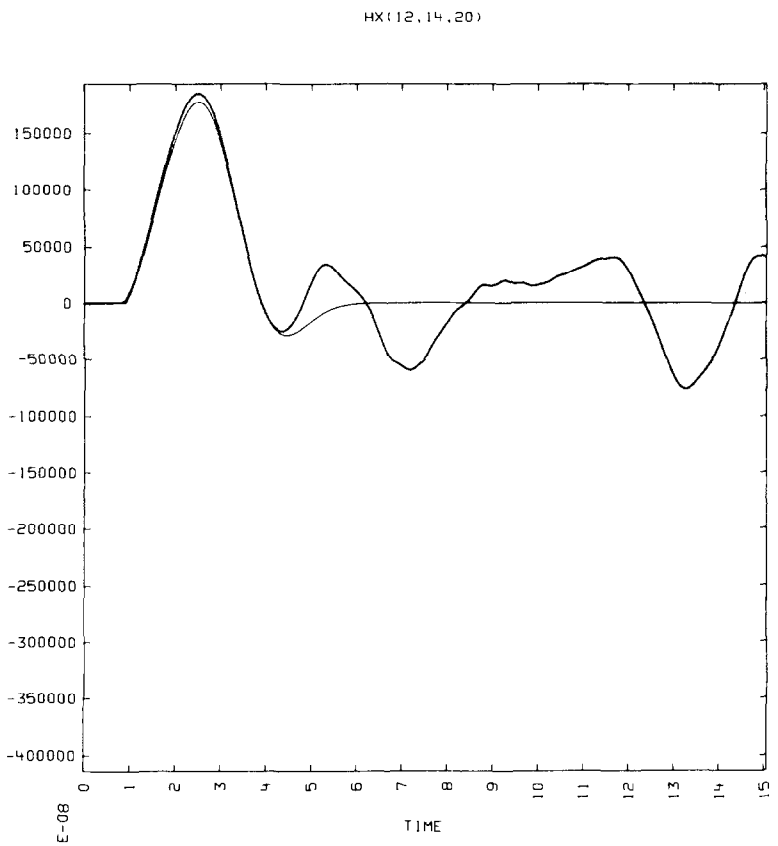

FIG. 12a. Comparison of the exact H_x values (—) with those calculated with a $29 \times 29 \times 29$ lattice and $E_{\tan} = 0$ outer boundary condition version of the THREDE code (···) at a point on Σ for a turned-on electric dipole.

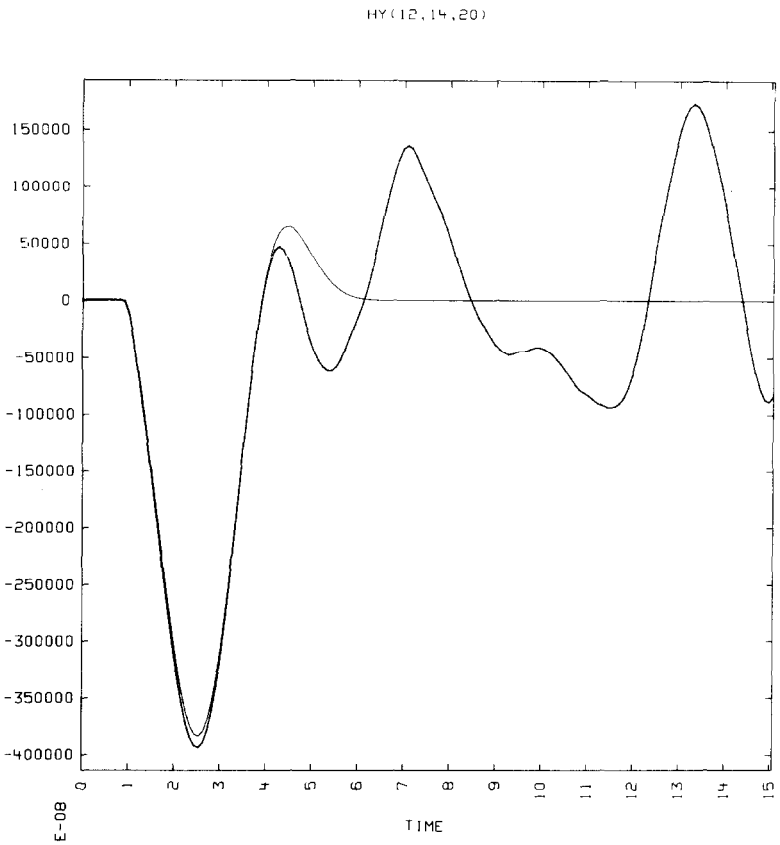

FIG. 12b. Comparison of the exact H_y values (—) with those calculated with a $29 \times 29 \times 29$ lattice and $E_{tan} = 0$ outer boundary condition version of the THREDE code (···) at a point on Σ for a turned-on electric dipole.

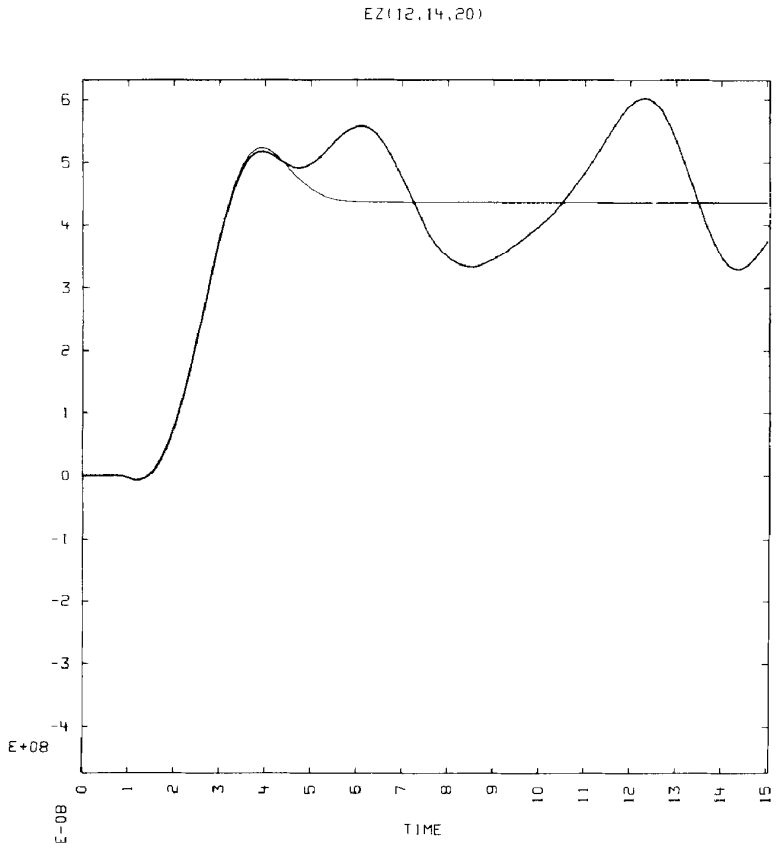

FIG. 12c. Comparison of the exact E_z values (—) with those calculated with a $29 \times 29 \times 29$ lattice and $E_{\tan} = 0$ outer boundary condition version of the THREDE code (···) at a point on Σ for a turned-on electric dipole.

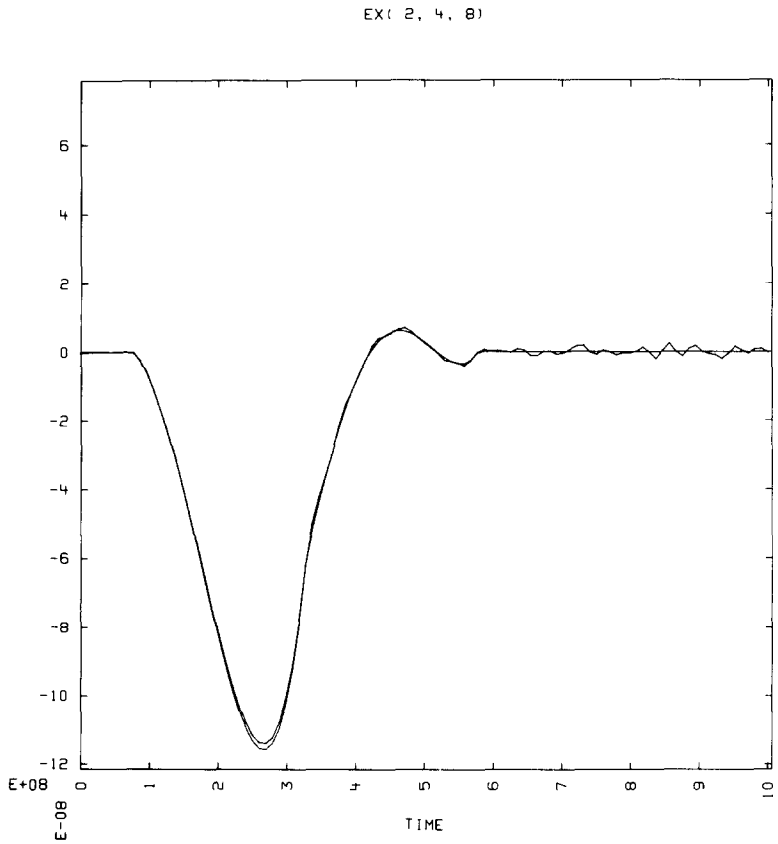

FIG. 13a. Comparison of the exact E_x values (—) with those calculated with the global lookback scheme (···) at an interior point for a turned-on-and-off electric dipole.

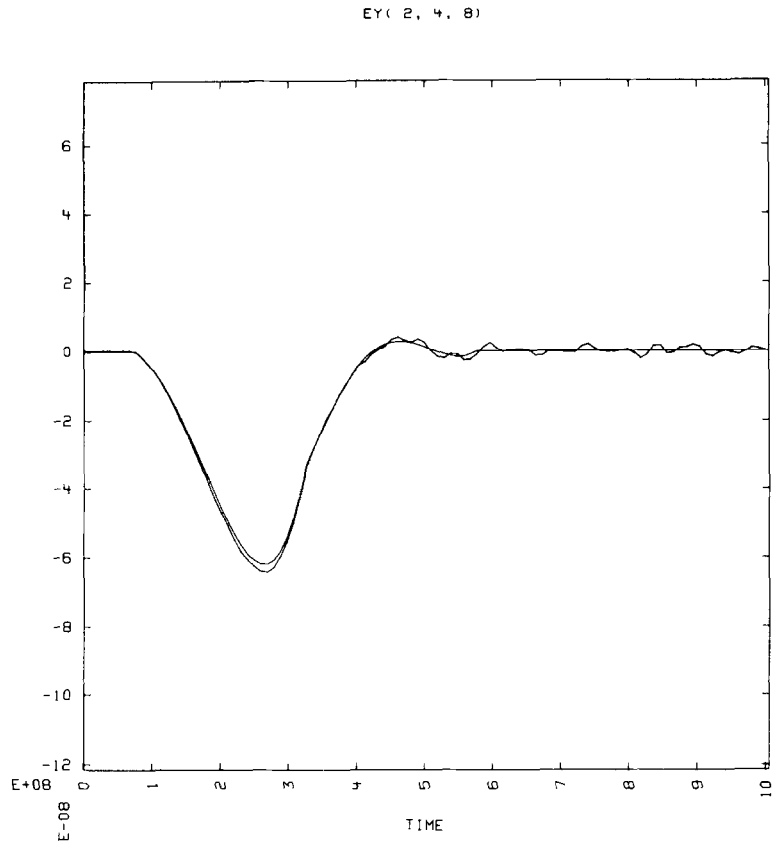

FIG. 13b. Comparison of the exact E_y values (—) with those calculated with the global lookback scheme (···) at an interior point for a turned-on-and-off electric dipole.

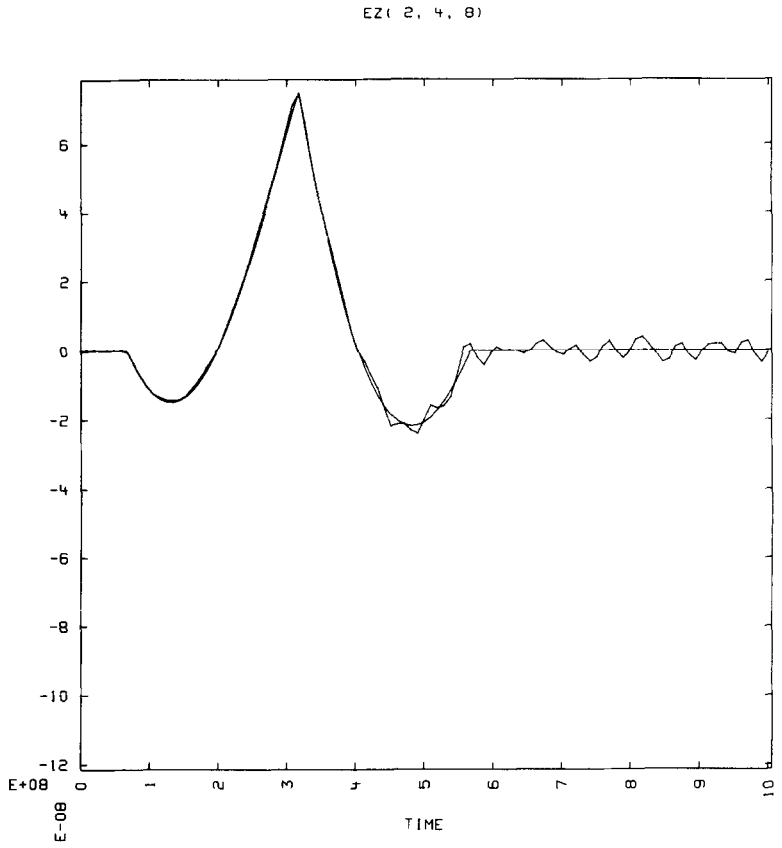

FIG. 13c. Comparison of the exact E_z values (—) with those calculated with the global lookback scheme (···) at an interior point for a turned-on-and-off electric dipole.

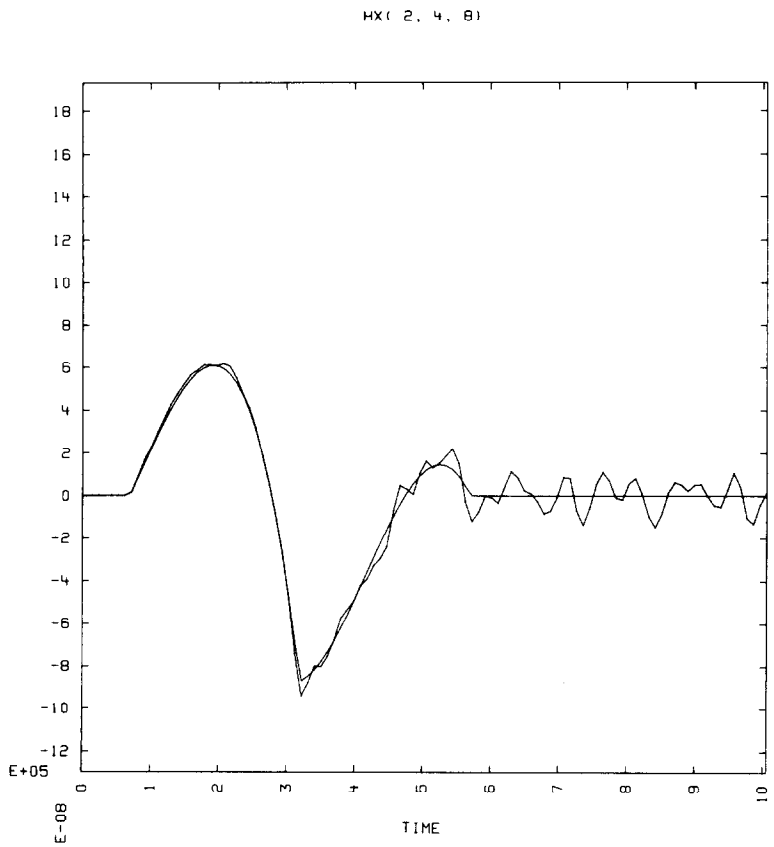

FIG. 13d. Comparison of the exact H_x values (—) with those calculated with the global lookback scheme (···) at an interior point for a turned-on-and-off electric dipole.

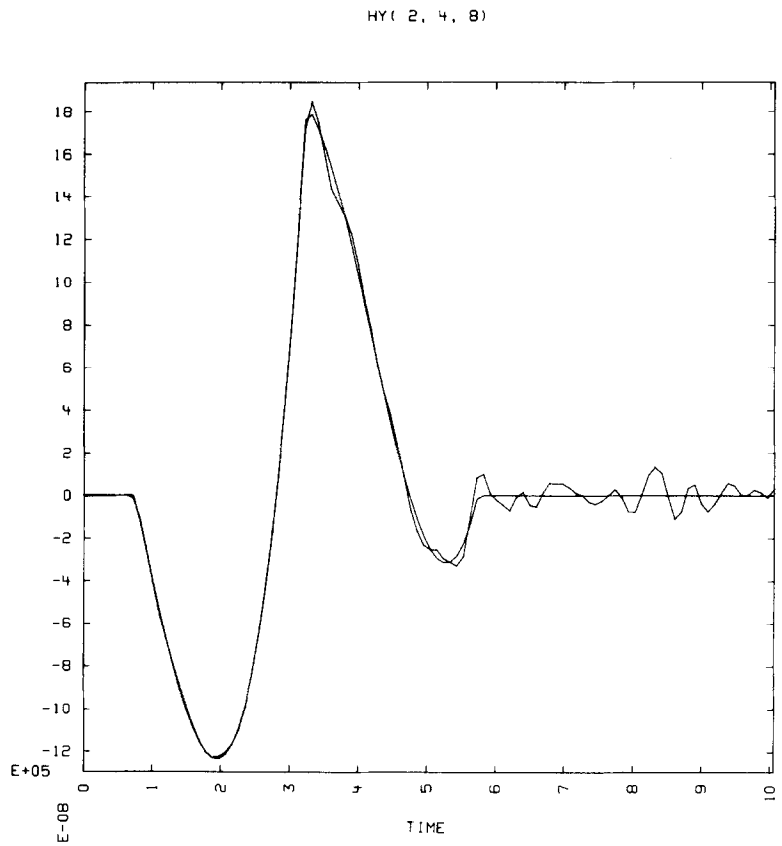

FIG. 13e. Comparison of the exact H_y values (—) with those calculated with the global lookback scheme (···) at an interior point for a turned-on-and-off electric dipole.

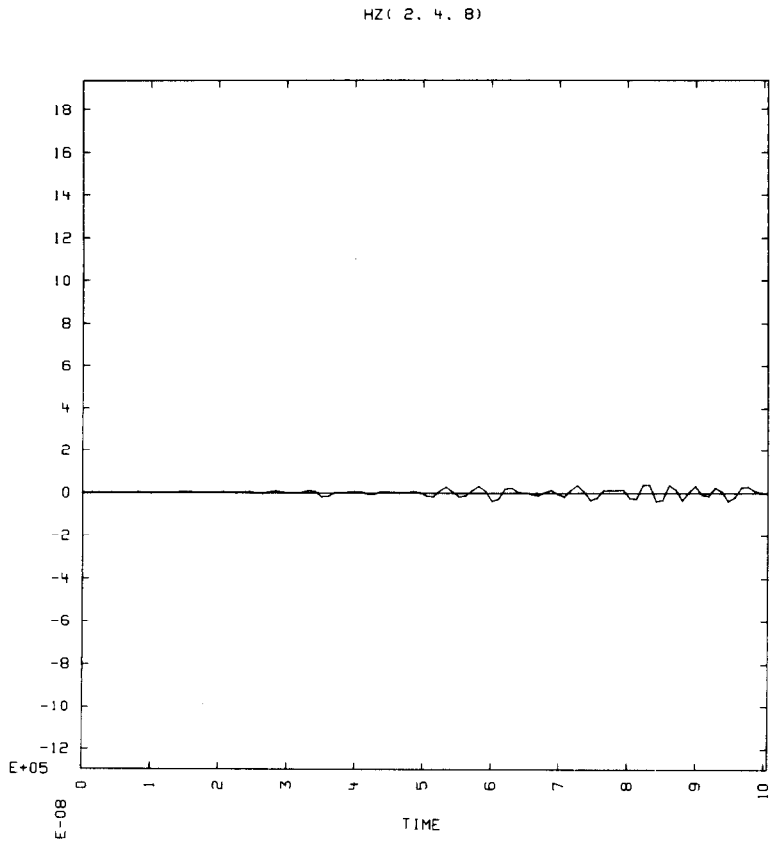

FIG. 13f. Comparison of the exact H_z values (—) with those calculated with the global lookback scheme (···) at an interior point for a turned-on-and-off electric dipole.

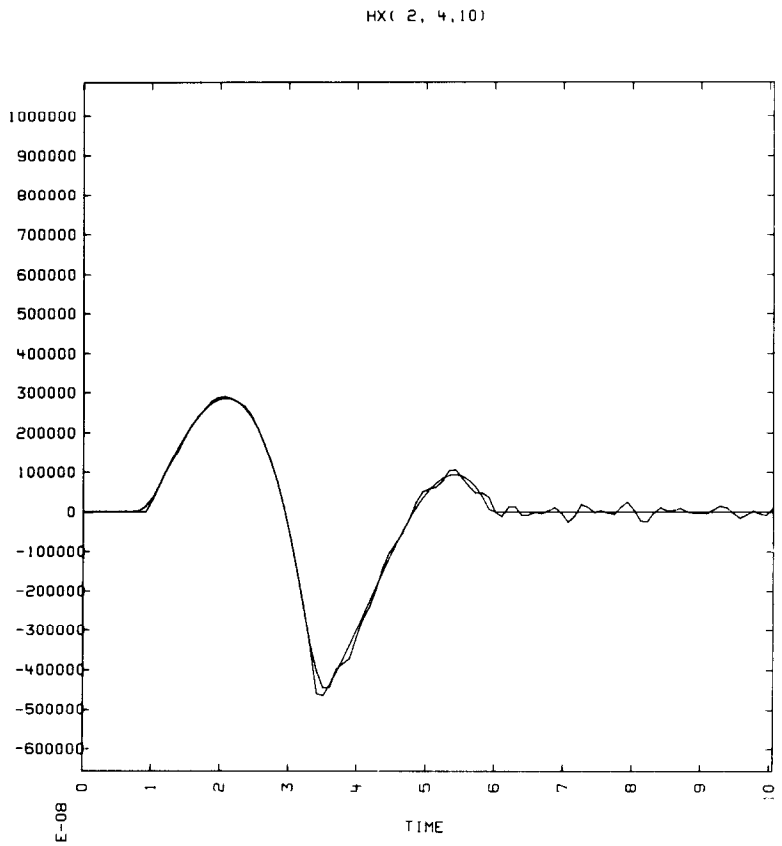

FIG. 14a. Comparison of the exact H_x values (—) with those calculated with the global lookback scheme (···) at a boundary point for a turned-on-and-off electric dipole.

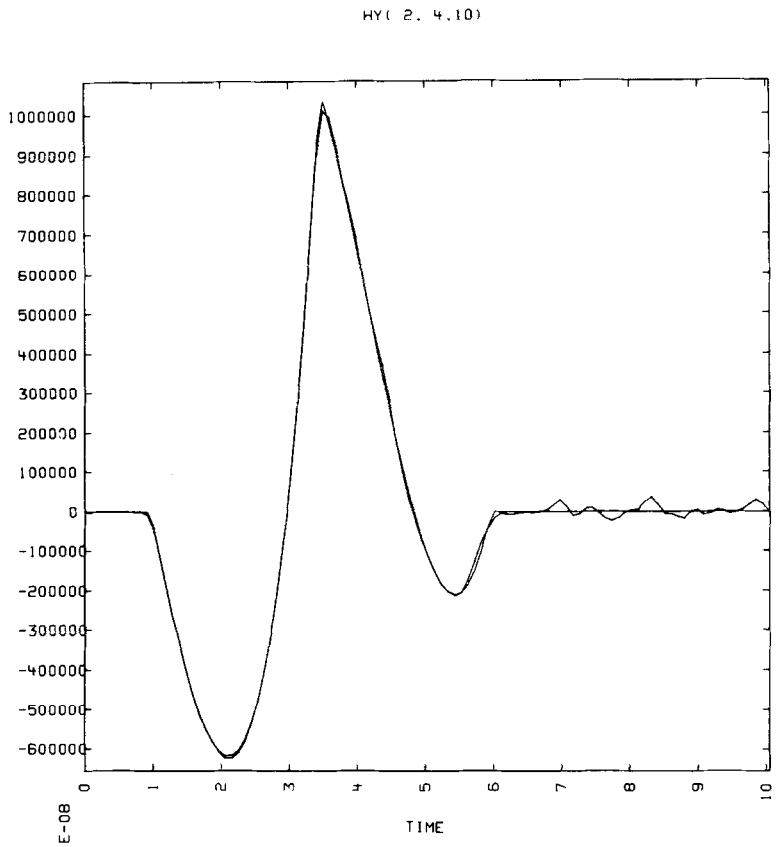

FIG. 14b. Comparison of the exact H_y values (—) with those calculated with the global lookback scheme (···) at a boundary point for a turned-on-and-off electric dipole.

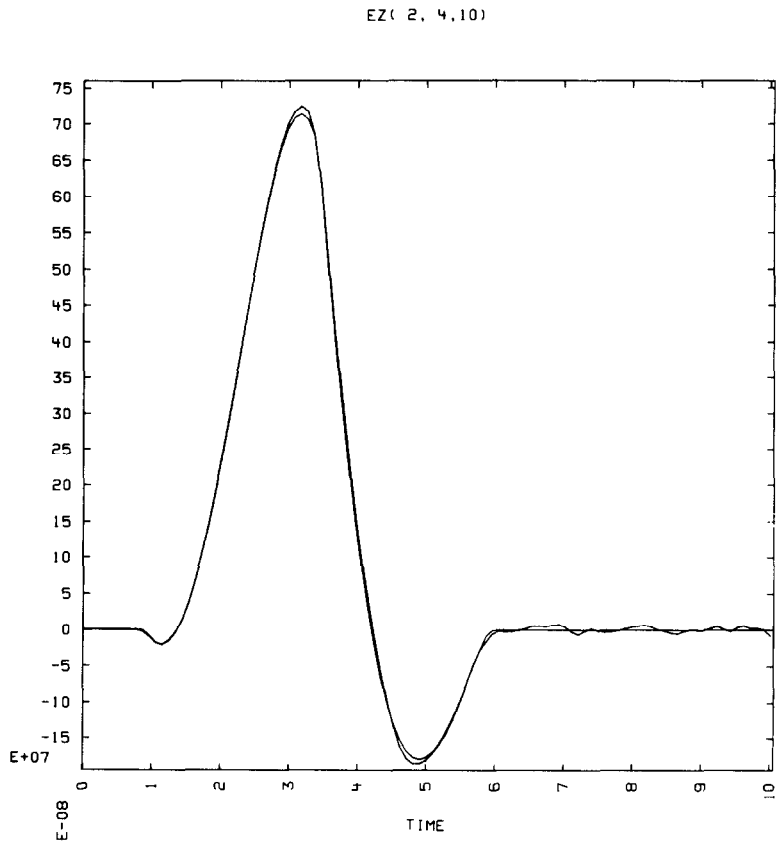

FIG. 14c. Comparison of the exact E_z values (—) with those calculated with the global lookback scheme (···) at a boundary point for a turned-on-and-off electric dipole.

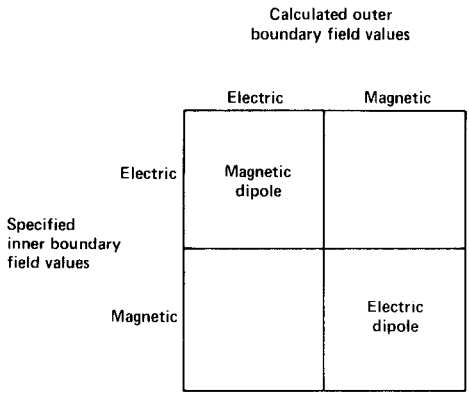

FIG. 15. Specific field value assignments necessary for modeling dipole fields with the global lookback scheme.

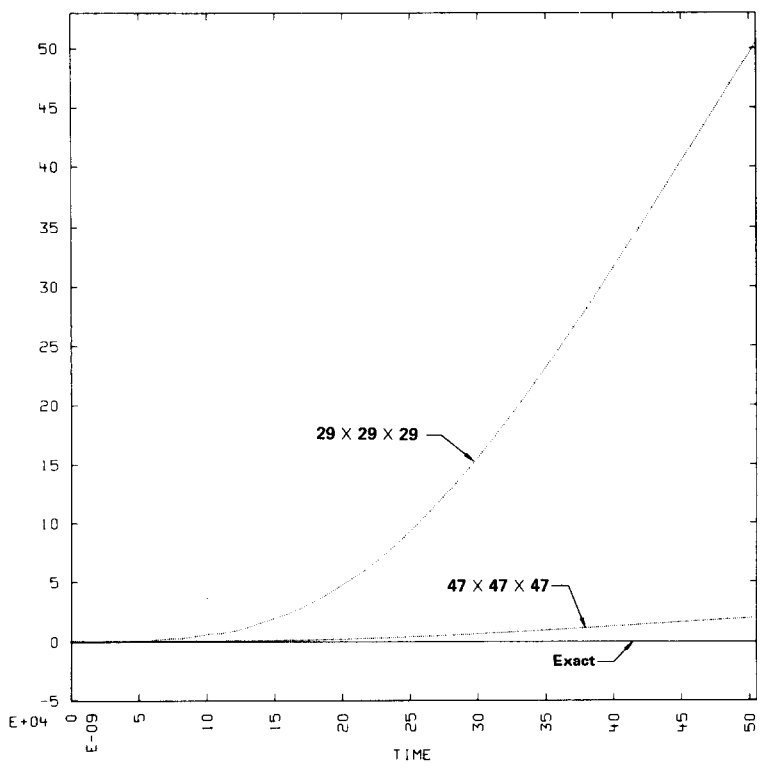

FIG. 16. Linear growth in an H_z component resulting from truncation errors (coarse lattice).

field values were significantly different from zero in the coarse lattice to act as sources in the magnetic field component difference equations. Although it is relatively small initially, the linear growth will eventually manifest itself strongly at later times. Refinement of the lattice greatly reduces the effects of this error as shown in Fig. 16. The linear growth in the H_z component when the electric dipole is modeled with electric field values on the inner boundary is illustrated. The curves were generated with the THREDE code with a $29 \times 29 \times 29$ and a $47 \times 47 \times 47$ lattice and with $E_{\tan} = 0$ outer boundary conditions. The behavior is indicative of truncation errors; it is not connected with the global lookback scheme.

5. Conclusions

An FD-TD lattice truncation scheme based upon an exact global lookback representation of the electromagnetic field has been developed. The success (in principle) of a numerical implementation of this global lookback scheme has been demonstrated. A considerable amount of optimization of the present algorithm and (most likely) several simplifying approximations will be necessary to make it an economically viable FD-TD technique. Several possible modifications of the code have been suggested. If it becomes economically competitive with the standard approximate approaches, however, it will be quite useful for a variety of open region problems. The ability to locate the lattice boundaries near to the regions of interest and yet model accurately late observation times and the exactness of its basic premise are all very attractive features of the global lookback scheme.

It has been demonstrated that electric (magnetic) dipoles can be modeled properly in an FD-TD lattice by specifying magnetic (electric) field values on an inner boundary surface closely surrounding the dipole. As summarized in Fig. 16, the global lookback scheme reproduced the solutions of the electric (magnetic) dipole problems only if the magnetic (electric) field components were also calculated on the outer boundary of the FD-TD lattice. Truncation errors appeared with any other specification of the fields on the inner and outer boundaries of the lattice. Those were due primarily to the large field variations characteristic of the singularities of the dipole field that were being modeled with a coarse lattice. It is felt that less severe field specifications on the inner boundary such as those due to an incident plane wave would not have developed the anomalies that were encountered.

APPENDIX A: Explicit Expressions of the Global Lookback Scheme Components

The explicit expressions of the electric field components employed in the global lookback scheme are

$$E_x(\bar{r},t)=\sum_{j=1}^{2}(-1)^j\int_{S_j^{xy}}dS_j^{xy}\frac{\theta(t_R)}{4\pi}\left\{[E_x+\tau\partial_tE_x]\frac{(\hat{z}\cdot\hat{R})}{R^2}\right.$$
$$\left.+[E_z+\tau\partial_tE_z]\frac{(\hat{x}\cdot\hat{R})}{R^2}+\frac{\mu_0}{R}[\partial_tH_y]\right\}$$
$$+\sum_{j=1}^{2}(-1)^j\int_{S_j^{zx}}dS_j^{zx}\frac{\theta(t_R)}{4\pi}\left\{[E_x+\tau\partial_tE_x]\frac{(\hat{y}\cdot\hat{R})}{R^2}\right.$$
$$\left.+[E_y+\tau\partial_tE_y]\frac{(\hat{x}\cdot\hat{R})}{R^2}-\frac{\mu_0}{R}[\partial_tH_z]\right\}$$
$$+\sum_{j=1}^{2}(-1)^j\int_{S_j^{yz}}dS_j^{yz}\frac{\theta(t_R)}{4\pi}\left\{2[E_x+\tau\partial_tE_x]\frac{(\hat{x}\cdot\hat{R})}{R^2}-[\bar{E}+\tau\partial_t\bar{E}]\cdot\frac{\hat{R}}{R^2}\right\}$$

$$E_y(\bar{r},t)=\sum_{j=1}^{2}(-1)^j\int_{S_j^{xy}}dS_j^{xy}\frac{\theta(t_R)}{4\pi}\left\{[E_y+\tau\partial_tE_y]\frac{(\hat{z}\cdot\hat{R})}{R^2}\right.$$
$$\left.+[E_z+\tau\partial_tE_z]\frac{(\hat{y}\cdot\hat{R})}{R^2}-\frac{\mu_0}{R}[\partial_tH_x]\right\}$$
$$+\sum_{j=1}^{2}(-1)^j\int_{S_j^{zx}}dS_j^{zx}\frac{\theta(t_R)}{4\pi}\left\{2[E_y+\tau\partial_tE_y]\frac{(\hat{y}\cdot R)}{R^2}-[\bar{E}+\tau\partial_t\bar{E}]\cdot\frac{\hat{R}}{R^2}\right\}$$
$$+\sum_{j=1}^{2}(-1)^j\int_{S_j^{yz}}dS_j^{yz}\frac{\theta(t_R)}{4\pi}\left\{[E_y+\tau\partial_tE_y]\frac{(\hat{x}\cdot\hat{R})}{R^2}\right.$$
$$\left.+[E_x+\tau\partial_tE_x]\frac{(\hat{y}\cdot\hat{R})}{R^2}+\frac{\mu_0}{R}[\partial_tH_z]\right\}$$

$$E_z(\bar{r},t)=\sum_{j=1}^{2}(-1)^j\int_{S_j^{xy}}dS_j^{xy}\frac{\theta(t_R)}{4\pi}\left\{2[E_z+\tau\partial_tE_z]\frac{(\hat{z}\cdot\hat{R})}{R^2}-[\bar{E}+\tau\partial_t\bar{E}]\cdot\frac{\hat{R}}{R^2}\right\}$$
$$+\sum_{j=1}^{2}(-1)^j\int_{S_j^{zx}}dS_j^{zx}\frac{\theta(t_R)}{4\pi}\left\{[E_z+\tau\partial_tE_z]\frac{(\hat{y}\cdot\hat{R})}{R^2}\right.$$
$$\left.+[E_y+\tau\partial_rE_y]\frac{(\hat{z}\cdot\hat{R})}{R^2}+\frac{\mu_0}{R}[\partial_tH_x]\right\}$$
$$+\sum_{j=1}^{2}(-1)^j\int_{S_j^{zx}}dS_j^{yz}\frac{\theta(t_R)}{4\pi}\left\{[E_z+\tau\partial_tE_z]\frac{(\hat{x}\cdot\hat{R})}{R^2}\right.$$
$$\left.+[E_x+\tau\partial_tE_x]\frac{(\hat{z}\cdot\hat{R})}{R^2}-\frac{\mu_0}{R}[\partial_tH_y]\right\},$$

where

S_1^{xy}: face of inner cube, where $z=\Delta z_1$,

S_2^{xy}: face of inner cube, where $z=N_z\,\Delta z-\Delta z_{N_z}$,

S_1^{zx}: face of inner cube, where $y = \Delta y_1$,

S_2^{zx}: face of inner cube, where $y = N_y \Delta y - \Delta y_{N_y}$,

S_1^{yz}: face of inner cube, where $x = \Delta x_1$,

S_2^{yz}: face of inner cube, where $x = N_x \Delta x - \Delta x_{N_x}$.

The magnetic field components are obtained readily from these expressions with the replacements $E \to H \to -E$ and $\mu_0 \to \varepsilon_0$.

APPENDIX B: A General Discretized Form of the Exact Global Lookback Field Representation

A general discretized form of the exact global lookback representation of the electromagnetic field is obtained as follows: Let the surface patch S_p be a zone or a combination of zones on S centered about the spatial lattice point $\bar{r}_p$ and let I_q be a time interval centered about the time lattice point t_q. Assume that the patches S_p $(p = 1,..., P)$ cover S and that the intervals I_q $(q = 1,..., Q)$ cover the time interval of interest. Let $\Phi_p(\bar{r})$ and $\Psi_q(t)$ be the characteristic functions of the surface S_p and of the time interval I_q; e.g., $\Phi_p(\bar{r}_p) = 1$ and $\Phi_p(\bar{r}) \equiv 0$ if $\bar{r}$ is not on S_p. The field components on S can then be discretized, for example, as

$$E_i(\bar{r}', \hat{t}) = \sum_{p=1}^{P} \sum_{q=1}^{Q} \Phi_p(\bar{r}')\, \Psi_q(\hat{t})\, E_i^{pq}, \tag{B.1}$$

where $E_i(\bar{r}_p, t_q) \equiv E_i^{pq}$. Thus, the global lookback expression (3.7) has the general form

$$E_i^{mn} = \sum_{j=1}^{3} \sum_{p=1}^{P} \sum_{q=1}^{Q} \{A_{ipq}^{jmn} E_j^{pq} + \mu_0 B_{ipq}^{jmn} H_j^{pq}\}, \tag{B.2}$$

where $\bar{r}_m$ is a point on Σ and $E_j(r_m, t_n) \equiv E_i^{mn}$, and where the coefficients

$$A_{ipq}^{jmn} = \hat{A}_i^j(\bar{r}_m, \bar{r}'; t_n)\{\Phi_p(\bar{r}')\, \Psi_q(t_n - r'/c)\} \tag{B.3}$$

$$B_{ipq}^{jmn} = \hat{B}_i^j(\bar{r}_m, \bar{r}'; t_n)\{\Phi_p(\bar{r}')\, \Psi_q(t_n - r'/c)\}. \tag{B.4}$$

Note that these terms reduce simply to integrals over the surface patch S_p; they are dependent only on the geometry and the choice of interpolation scheme. The expression dual to (3.14) is

$$H_i^{mn} = \sum_{j=1}^{3} \sum_{p=1}^{P} \sum_{q=1}^{Q} \{A_{ipq}^{jmn} H_j^{pq} - \varepsilon_0 B_{ipq}^{jmn} E_j^{pq}\}. \tag{B.5}$$

Finally, note that Eqs. (3.7) and (3.12) can be combined into a single matrix equation

$$F(\bar{r}, t) = \hat{G}(\bar{r}, \bar{r}'; t)\, F(\bar{r}', \hat{t}), \tag{B.6}$$

where F is the six-component field column vector

$$F = \begin{bmatrix} \bar{E} \\ \bar{H} \end{bmatrix} \tag{B.7}$$

and $\hat{G}$ is the 6×6 matrix operator

$$\hat{G} = \begin{pmatrix} \hat{A} & \mu_0 \hat{B} \\ -\varepsilon_0 \hat{B} & \hat{A} \end{pmatrix}, \tag{B.8}$$

where the 3×3 operators $\hat{A}$ and $\hat{B}$ have the components $\hat{A}_i^j$ and $\hat{B}_i^j$. The operator $\hat{G}$ represents a propagator of the fields defined over S to those defined over Σ. The discretized form of (B.6) is simply

$$F^{mn} = \sum_{p=1}^{P} \sum_{q=1}^{Q} G_{pq}^{mn} F^{pq}, \tag{B.9}$$

where $F^{mn} = F(\bar{r}_m, t_n)$, $F^{pq} = F(\bar{r}_p, t_q)$, and

$$G_{pq}^{mn} = \begin{pmatrix} A_{pq}^{mn} & \mu_0 B_{pq}^{mn} \\ -\varepsilon_0 B_{pq}^{mn} & A_{pq}^{mn} \end{pmatrix}, \tag{B.10}$$

where, for example, the matrix A_{pq}^{mn} has the components A_{ipq}^{jmn}. Expression (B.9) is the general discretized form of the exact global lookback field representation.

APPENDIX C: Components of the Electric Dipole Field

The components of the electric dipole field are

$$E_x(x, y, z, t) = \frac{xz}{4\pi\varepsilon_0 r^5} \{3[f + \tau\partial_t f] + \tau^2[\partial_t^2 f]\},$$

$$E_y(x, y, z, t) = (y/x)\, E_x(x, y, z, t),$$

$$E_z(x, y, z, t) = \frac{1}{4\pi\varepsilon_0 r^5} \{(2z^2 - (x^2 + y^2))[f + \tau\partial_t f] - (x^2 + y^2)\tau^2[\partial_t^2 f]\},$$

$$H_x(x, y, z, t) = -\frac{y}{4\pi r^3} [\partial_t f + \tau\partial_t^2 f],$$

$$H_y(x, y, z, t) = -(x/y)\, H_x(x, y, z, t),$$

$$H_z(x, y, z, t) = 0,$$

where

$$r = (x^2 + y^2 + z^2)^{1/2}.$$

REFERENCES

1. G. KRON, *Proc. IRE* **32** (1944), 289.
2. K. S. YEE, *IEEE Trans. Antennas Propag.* **AP-14** (1966), 302.
3. R. HOLLAND, *IEEE Trans. Nucl. Sci.* **NS-24** (1977), 2416.
4. R. HOLLAND, L. SIMPSON, AND K. S. KUNZ, *IEEE Trans. Electromagn. Compat.* **EMC-22** (1980), 203.
5. R. HOLLAND AND L. SIMPSON, *IEEE Trans. Electromagn. Compat.* **EMC-23** (1981), 88.
6. D. E. MEREWETHER AND R. FISHER, EMA Final Report, EMA-79-R-4, 1980.
7. D. E. MEREWETHER, R. FISHER, AND F. W. SMITH, EMA Report, EMA-80-R-11, 1980.
8. T. A. TUMOLILLO AND J. P. WONDRA, *IEEE Trans. Nucl. Sci.* **NS-24** (1977), 82.
9. T. A. TUMOLILLO, J. P. WONDRA, J. BOMBARDT, G. MERKEL, AND D. SPOHN, *IEEE Trans. Nucl. Sci.* **NS-24** (1977), 70.
10. A. TAFLOVE AND M. E. BRODWIN, *IEEE Trans. Microwave Theory Tech.* **MTT-23** (1975), 623.
11. A. TAFLOVE, *IEEE Trans. Electromagn. Compat.* **EMC-22** (1980), 191.
12. A. TAFLOVE, IITRI Final Report, RADC-TR-80-251, 1980
13. A. TAFLOVE AND K. R. UMASHANKAR, "Solution of Complex Electromagnetic Penetration and Scattering Problems in Unbounded Regions," Reprint of paper presented at 1981 URSI Conference, Los Angeles, Calif.
14. J. GILBERT, MRC Report, MRC-R-296, 1976.
15. K. D. GRANZOW, Dikewood Industries Final Report, AFWL-TR-78-266, 1980.
16. I. KATZ, D. PARKS, A. WILSON, AND J. HARVEY, S^3 Topical Report, SSS-R-76-2934, 1976.
17. C. L. LONGMIRE, AFWL Theoretical Notes, AFWL-EMP-2-4, TN-70, 1971.
18. W. D. SMITH, *J. Comput. Phys.* **15** (1974), 492.
19. E. L. LINDMAN, *J. Comput. Phys.* **18** (1975), 66.
20. B. ENGQUIST AND A. MAJDA, *Math. Comput.* **31** (1977), 629.
21. D. S. JONES, "The Theory of Electromagnetism," pp. 43–45, Macmillian, New York, 1964.
22. B. H. MCDONALD AND A. WEXLER, *IEEE Trans. Microwave Theory Tech.* **MTT-20** (1972), 841.